TU Delft

Delft University of Technology

Document Version
Final published version

Citation (APA)
Zhu, Y., Hood, Z. D., Paik, H., Groszewicz, P. B., Emge, S. P., Sayed, F. N., Sun, C., Balaish, M., Ehre, D., Rupp, J. L. M., & More Authors (2024). Highly disordered amorphous Li-battery electrolytes. *Matter*, *7*(2), 500-522. https://doi.org/10.1016/j.matt.2023.12.004

Important note
To cite this publication, please use the final published version (if applicable).
Please check the document version above.

Copyright
In case the licence states “Dutch Copyright Act (Article 25fa)”, this publication was made available Green Open Access via the TU Delft Institutional Repository pursuant to Dutch Copyright Act (Article 25fa, the Taverne amendment). This provision does not affect copyright ownership.
Unless copyright is transferred by contract or statute, it remains with the copyright holder.

Sharing and reuse
Other than for strictly personal use, it is not permitted to download, forward or distribute the text or part of it, without the consent of the author(s) and/or copyright holder(s), unless the work is under an open content license such as Creative Commons.

Takedown policy
Please contact us and provide details if you believe this document breaches copyrights.
We will remove access to the work immediately and investigate your claim.

This work is downloaded from Delft University of Technology.

Green Open Access added to TU Delft Institutional Repository

'You share, we take care!' - Taverne project

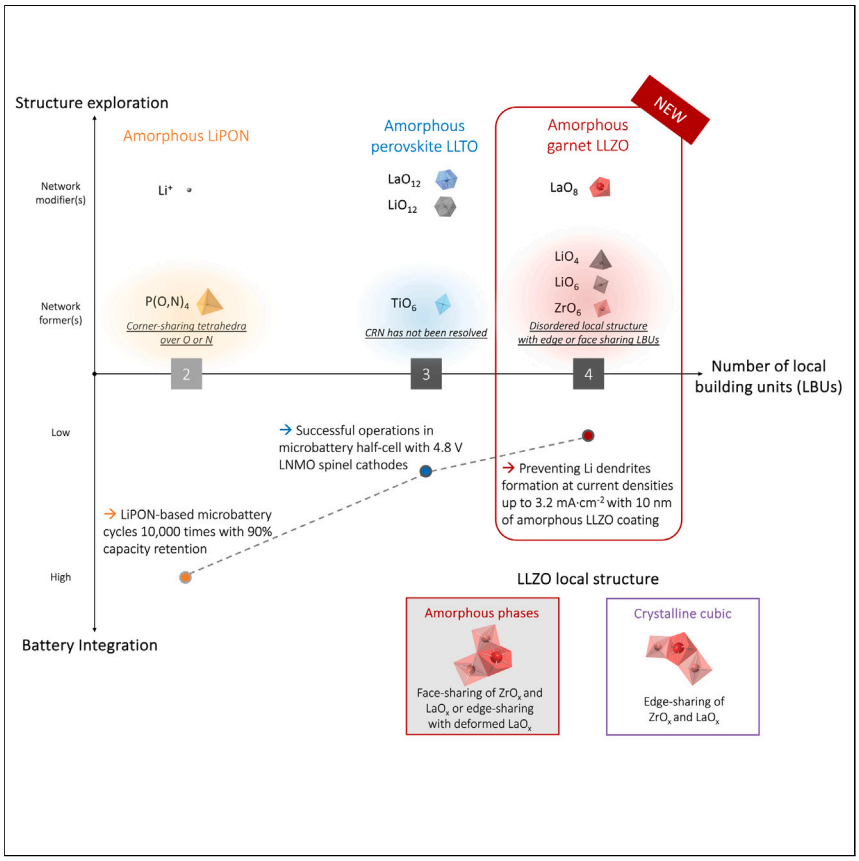
https://www.openaccess.nl/en/you-share-we-take-care

Otherwise as indicated in the copyright section: the publisher is the copyright holder of this work and the author uses the Dutch legislation to make this work public.

Matter

Article

Highly disordered amorphous Li-battery electrolytes



"Medium-entropy" amorphous Li garnets, with ≥4 local bonding units (LBUs), exhibit potential as solid-state electrolytes in hybrid or all-solid-state batteries owing to their grain-boundary-free nature and low-temperature synthesis requirement. Investigation of the local structure reveals edge- and face-sharing LBUs, deviating from the classic Zachariasen rules. In these structures, Li and Zr act as the network formers and La as network modifier, with enhanced Li dynamics observed for smaller Li–O and Zr–O coordination.

Yuntong Zhu, Zachary D. Hood, Haemin Paik, ..., Igor Lubomirsky, Clare P. Grey, Jennifer L.M. Rupp

jrupp@mit.edu

Highlights

Amorphous Li garnets consist of ≥4 edge- and face-sharing local bonding units

Li and Zr are identified as the network formers and La as network modifier

Maxima in Li^+ conductivity are observed for smaller Li–O and Zr–O coordination

Amorphous Li-garnet structures are contextualized toward existing glassy electrolytes

3 Understanding
Dependency and conditional studies on material behavior

Zhu et al., Matter 7, 500–522
February 7, 2024 © 2023 Elsevier Inc.
https://doi.org/10.1016/j.matt.2023.12.004

CellPress

Matter

Article

Highly disordered amorphous Li-battery electrolytes

Yuntong Zhu,[1] Zachary D. Hood,[1] Haemin Paik,[1] Pedro B. Groszewicz,[2,3] Steffen P. Emge,[2] Farheen N. Sayed,[2] Chengjun Sun,[4] Moran Balaish,[1,5,6] David Ehre,[7] Lincoln J. Miara,[8] Anatoly I. Frenkel,[9,10] Igor Lubomirsky,[7] Clare P. Grey,[2] and Jennifer L.M. Rupp[1,5,6,11,12,*]

SUMMARY

"Medium-entropy" highly disordered amorphous Li garnets, with ≥4 unique local bonding units (LBUs), hold promise for use as solid-state electrolytes in hybrid or all-solid-state batteries owing to their grain-boundary-free nature and low-temperature synthesis requirement. Through this work, we resolved the local structure of amorphous Li garnet and understood their implication for Li dynamics. These medium-entropy amorphous structures possess unique characteristics with edge- and face-sharing LBUs, not conforming to the classic Zachariasen glass formation rules, and can be synthesized in a wide but processing-friendly temperature range (<680°C). Within these amorphous structures, Li and Zr are identified as the network formers and La as network modifier, with maxima in Li dynamics observed for smaller Li–O and Zr–O coordination; this structure understanding serves as a baseline for identifying additional network formers to further modulate Li transport. Our insight provides fundamental guidelines for the structure and phase design for amorphous Li garnets and paves the way for their integration in next-generation batteries.

INTRODUCTION

With the increasing demand for electric vehicles and portable electronic devices, breakthroughs to further improve the energy density and cycle life of battery technologies are necessary.[1–4] Extensive research efforts have focused on reviving lithium (Li) metal as the ultimate anode for "beyond Li-ion batteries" owing to the outstanding specific capacity of Li metal (3,860 mAh g^{-1}) and the low electrochemical potential (−3.04 V vs. standard hydrogen electrode).[5] Replacing the conventional graphite anode with Li should in principle provide a feasible path for increasing the specific energy density by 35–350 Wh kg^{-1} at the pack level.[3,6] However, gas and heat evolution during Li-dendrite growth and the electrochemical instability between Li metal and conventional liquid electrolytes remain major concerns.[7] Solid-state electrolytes, such as Li-garnet-type $Li_7La_3Zr_2O_{12-\delta}$ (LLZO)[8–14] and Li phosphorous oxynitride glass $Li_xPO_yN_z$ (LiPON),[15,16] have been regarded as the key contenders for use in Li-metal batteries with increased resistance toward dendrite growth while providing high Li-ion conductivities.[2] The majority of these solid-state electrolytes, such as LLZO ceramics, exhibit their highest Li conductivity in cubic polycrystalline phase with a large grain-boundary volume, which, in turn, is more susceptible to Li-dendrite growth and battery failure. Electron microscopy[17–19] and opto-mechanical microscopy[20] studies have revealed that Li preferentially deposits along the grain boundary for LLZO. This behavior in part stems from the variation of the transference number, which can increase the electronic conductivity at different localities of the grain boundary and thus promote Li-dendrite propagation.[18] A recent study also suggests

PROGRESS AND POTENTIAL

Amorphous Li oxides are promising solid-state electrolytes for use in hybrid or all-solid-state oxide- and sulfide-based batteries as separators or protective layers. These amorphous Li-ion conductors possess an intrinsic grain-boundary-free nature and require significantly lower temperatures for synthesis as compared to their crystalline counterparts. Different from lower-entropy amorphous conductors such as LiPON and Ohara glass, highly disordered amorphous conductors, such as amorphous Li garnets, exhibit an unusually high number of local bonding units (LBUs) and offer a much wider opportunity to tune the structure and transport properties. These medium-entropy phases do not follow the classic Zachariasen glass rules and require a proper fundamental description. Here, a multi-faceted investigation has been carried out to resolve the structure of these medium-entropy amorphous Li-garnet phases, identify major roles of the LBUs, and understand their implications on Li dynamics. We contextualize and classify these medium-entropy amorphous conductors toward existing glassy electrolytes. Technologically, we see the promise of our contribution in resolving the medium-entropy

CellPress

that cubic polymorphism (i.e., 220 vs. 230 space group cubic phase) could be related to dendrite nucleation and propagation in polycrystalline cubic LLZO due to local stress formation around 230 space group grains.[21,22] While many other theories exist implying the vulnerability of grain boundaries, the exact cause of Li-dendrite formation and propagation, remains to be clarified. Remarkably, amorphous Li-ion conductors such as LiPON thus far represent an exception, being inherently grain-boundary-free and offering the best cycling stability, i.e., maintained for more than 10,000 cycles and at <10% degradation with a Li-metal anode.[23] It has been argued that LiPON forms a thin electronically insulating but stable interphase layer composed of Li_3PO_4, Li_3N, Li_3P, and Li_2O toward pure Li at lower voltages, contributing positively to the high cycle life.[24–26] In addition to LiPON, there are many additional alternative amorphous Li-conducting materials, such as amorphous Li garnets (Figures 1B and 1C), and opportunities for new phase definition and synthesis are manifold. These materials possess several attractive characteristics, such as their relatively low manufacturing temperature (ranging from room temperature to 600°C), which facilitates co-synthesis with Co-substituted or even Co-free cathodes (e.g., $LiNiMnCoO_2$, $LiNiCoAlO_2$, and $LiFePO_4$) that are often unstable at standard electrolyte sintering temperatures. Alternatively, they can be applied as protective coatings (electrode-electrolyte interfacial layers) toward Li anodes and other Li-free anode concepts, bridging the electrochemical stability voltage gap with liquid electrolytes or catholytes and preventing uneven interfacial reactions, which may later lead to uneven Li stripping/plating (Figure 1A). An earlier study reported that by applying a 10-nm amorphous Li-garnet protective coating on both sides of a cubic Li-garnet pellet, a 4-fold increase in critical current density (CCD) from 0.32 to 1.3 mA cm^{-2} can be achieved.[27] In principle, an oxide-based protective coating can also be extended to sulfide-based solid-state batteries to bridge the large electrochemical stability voltage gap between sulfide-based electrolytes (that generally have electrochemical stability windows <1 V)[28] and a Li anode. Their ultimate usage either as effective Li-electrolyte separators or thin protective layers remains to be explored, providing new pathways for battery designs.

In this work, we explore the fascinating nature of highly disordered amorphous Li-garnet battery conductors, which has an unusually high number of local bonding units (LBUs), generally beyond four, that affect Li transfer. Although they have been successfully implemented in solid-state batteries, the nature of the amorphous Li-garnet structures remains unresolved and requires a proper fundamental description. These medium-entropy amorphous Li garnets can exist in various phases and differ substantially from lower-entropy amorphous conductors such as Ohara glass, as the amorphous Li garnets discussed here are technically not even "glasses" based on the Zachariasen glass theory, and the high number of LBUs ($\geq$4) offer a much wider opportunity to tune the structure and transport properties. In this study, the synthesis and local amorphous structure vs. Li migration interaction are studied, and the critical role of LBUs in determining network characteristics is explained for amorphous Li garnets. In addition, we aim to contextualize and classify these highly disordered amorphous Li-garnet conductors for the first time compared with existing non-Zachariasen amorphous electrolytes in the battery field. Technologically, these fundamental efforts provide blueprints for how to further modify these materials with dopants and synthesis routes for phase tailoring in follow-up studies.

RESULTS AND DISCUSSION

Bringing some order into disordered amorphous Li solid-battery electrolytes

We introduce in Figure 1B the varied range of existing non-Zachariasen amorphous Li-ion conducting oxides as well as the concepts of LBUs and network formers vs.

amorphous structure of Li garnets to guide materials and battery designs with further enhanced safety and lifetime.

[1]Department of Materials Science and Engineering, Massachusetts Institute of Technology, Cambridge, MA 02139, USA

[2]Yusuf Hamied Department of Chemistry, University of Cambridge, CB2 1EW Cambridge, UK

[3]Department of Radiation Science and Technology, Delft University of Technology, 2629 JB Delft, the Netherlands

[4]Advanced Photon Source, Argonne National Laboratory, Lemont, IL 60439, USA

[5]Department of Chemistry, Technical University Munich, 85748 Garching, Germany

[6]TUMint. Energy Research GmbH, Lichtenbergstr. 4, 85747 Garching, Germany

[7]Department of Molecular Chemistry and Materials Science, Weizmann Institute of Science, Rehovot 76100, Israel

[8]Advanced Materials Lab, Samsung Semiconductor, Inc., 10 Wilson Rd., Cambridge, MA 02138, USA

[9]Chemistry Division, Brookhaven National Laboratory, Upton, NY 11973, USA

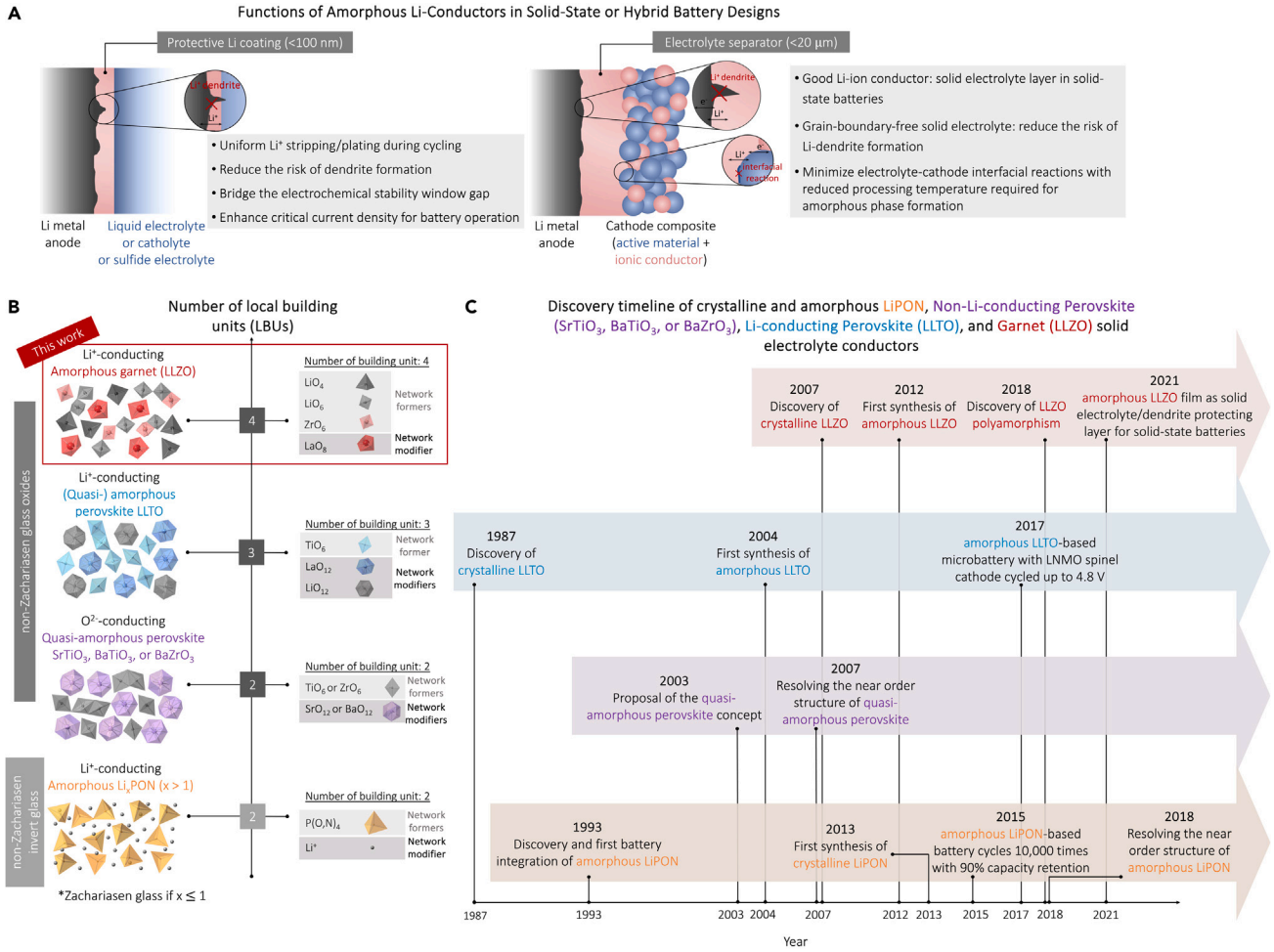
[10]Department of Materials Science and Chemical Engineering, Stony Brook University, Stony Brook, NY 11794, USA

[11]Department of Electrical Engineering and Computer Science, Massachusetts Institute of Technology, Cambridge, MA 02139, USA

[12]Lead contact

*Correspondence: jrupp@mit.edu

https://doi.org/10.1016/j.matt.2023.12.004



D

Materials	Li-phosphate glass LiPON	Quasi-amorphous perovskite $SrTiO_3$, $BaTiO_3$, or $BaZrO_3$	(Quasi-) amorphous perovskite LLTO	Amorphous garnet LLZO
Number of LBUs	2	2	3	4
	$[P(N,O)_4]$ and Li^+	$[TiO_6]$ or $[ZrO_6]$, and $[SrO_{12}]$ or $[BaO_{12}]$	$[TiO_6]$, $[LaO_{12}]$, and $[LiO_{12}]$	$[LiO_4]$, $[LiO_6]$, $[ZrO_6]$, and $[LaO_8]$
LBUs connection	Corners	Corners, Edges, Faces	Unknown	Unknown
Zachariasen's glass?	No	No	No	No
Known conduction mechanism	Yes	Yes	No	No
	Li hopping over interstitial sites	Under- and over-bonded O^{2-} anions enhance ion mobility		
Implement in batteries	Yes	No	Yes	Yes

Figure 1. Discovery and development of amorphous Li^+ solid electrolytes

(A) Functions of amorphous Li-ion conductors in solid-state or hybrid battery designs.

(B) Newly developed classification of amorphous local structure for $Li^+(O^{2-})$-ion conductors based on the number of local bonding units (LBUs) ranging from 2 to 4. Each LBU in an amorphous structure is identified as either a network modifier or a network former, based on its structural role. Among the amorphous conductors, LiPON is (in most compositions) a non-Zachariasen invert glass with $P(O,N)_4$ as a network former and interstitial Li^+ as a network modifier. Note that a special case of LiPON with ~1:1 ratio of Li^+ to $P(O,N)_4$ can be considered as a Zachariasen glass. Quasi-amorphous O^{2-}-conducting perovskites ($SrTiO_3$, $BaTiO_3$, or $BaZrO_3$), amorphous Li^+-conducting perovskite LLTO, and amorphous garnet LLZO are also classified as non-Zachariasen glasses but with more complicated CRNs. In quasi-amorphous O^{2-}-conducting perovskites ($SrTiO_3$, $BaTiO_3$, or $BaZrO_3$), TiO_6 and ZrO_6 are identified as network formers, and SrO_{12} and BaO_{12} are identified as network modifiers.[29–32] In amorphous Li^+-conducting perovskite LLTO, TiO_6 is identified as a network former, and LaO_{12} and LiO_{12} are identified as network modifiers. In amorphous Li^+-conducting garnet LLZO, we identified in this study that LiO_4, LiO_6, and ZrO_6 are network formers and that LaO_8 is a network modifier, based on the atomic radius of the La cation and the probed LBU connection.

(C) Discovery and battery-application timeline of crystalline and amorphous LiPON,[16,23,33,34,35] O^{2-}-conducting perovskites ($SrTiO_3$, $BaTiO_3$, or $BaZrO_3$),[29–32] Li^+-conducting perovskite LLTO,[36–38,39] and Li^+-conducting garnet LLZO solid-electrolyte conductors.[13,27,40,41]

(D) Summary of structure properties, conduction mechanism, and battery applications of amorphous LiPON, quasi-amorphous O^{2-}-conducting perovskites ($SrTiO_3$, $BaTiO_3$, or $BaZrO_3$), amorphous Li^+-conducting perovskite LLTO, and amorphous Li^+-conducting garnet LLZO.

network modifiers. These electrolytes constitute two or more cation polyhedra LBUs in the continuous random networks (CRNs). Depending on the arrangement and structural roles in CRNs, LBUs can be distinguished as a "network former" or "network modifier"[42]: (1) network formers facilitate the formation of a CRN by forming covalent bonds via bridging oxygen or other available atoms (e.g., nitrogen in LiPON); (2) network modifiers alter the CRN through the formation of ionic bonds with non-bridging oxygen atoms. The form in which the LBUs link, their distances, and their connection affect the ionic transport. As a second parameter, it is relevant to define whether an amorphous Li-ion conductor can be classified as a Zachariasen glass. Any solid amorphous oxide constituting a majority of network-former LBUs with network-former coordination of 3 or 4 and solely corner sharing (forming covalent bonds) via bridging oxygens can be viewed as a Zachariasen glass. To provide some material examples, Li-sulfide solid electrolytes, e.g., $(100 - x)Li_2S - xP_2S_5$, are true Zachariasen glasses with PS_4 tetrahedra being the corner-sharing network former and Li^+ being the network modifier.[43,44]

In addition to Zachariasen glasses, there are many non-Zachariasen amorphous structures that provide far more complicated CRNs with higher structural entropy, such as metallic glasses,[45,46] disordered ceramics,[47] and invert ion-conducting glasses.[48] Specifically, invert glasses attract attention in the battery field as they can offer high Li^+ conductivity thanks to their network-modifier-dominated structures and ionic-bonding characteristics.[48] For instance, the majority of LiPON can be categorized as a non-Zachariasen invert glass because it contains less network former $P(N,O)_4$ than the network modifier Li^+ in the CRN, not conforming to the classic Zachariasen glass formation rules any longer.[48] Its glass structure and physical properties are largely determined by the network modifier cations, Li^+, and the predominant ionic bonds.

To lay the groundwork, we classify the various known non-Zachariasen amorphous Li^+-(O^{2-})-conducting oxides according to the number of LBUs in Figure 1B. We briefly summarize the implications of the number of LBUs on the structure coordination and transport properties and herewith propose this general classification to the field for further discussion of the definition.

Low number of LBUs for solid-state conductors (LBUs = 2) forming either a non-Zachariasen invert glass or a classic Zachariasen glass

LiPON consists of two types of LBU, i.e., $P(N,O)_4$ tetrahedra as a network former and Li^+ as a network modifier, and can be classified as either a non-Zachariasen invert glass or a classic Zachariasen glass depending on the network former-to-modifier ratios. In most cases, LiPON consists of more network modifier Li^+ than network former $P(N,O)_4$ and can be considered as a non-Zachariasen invert glass. The network former $P(N,O)_4$ is surrounded by a lithia matrix with non-bridging O or N or held together by corner-sharing N or O atoms (Figure 1B).[33] The ionic interactions between Li^+ and oxoanions become essential in determining the CRNs and glass properties.[48] For $P(N,O)_4$ with corner-shared N, bridging N (double bond) and apical N (single bond) prevail in the CRN when chemically satisfying $x < 1$ for $Li_3PO_{(4-x)}N_{(2x/3)}$.[33] The presence of N bridges destabilizes the Li-Li interaction because of its covalent bonds with P, thus enhancing the Li-ion mobility,[34] and is the essence of modulating conductivities to nearly 10^{-5} S cm^{-1} under ambient conditions in the given CRN.[49] In the special case of LiPON, the network former-to-modifier ratio is ~1:1; by definition, this less visited LiPON structure can be classified as a true Zachariasen glass.[50,51] Techno-historically speaking, it is evident that over the last two decades the invert glass LiPON has been the best investigated amorphous

Li-ion conductor and has been integrated as a solid-state electrolyte in batteries, demonstrating the best long-term performance and compatibility with Li-metal anode thus far (Figure 1C).[23]

Low-to-moderate number of LBUs for solid-state conductors (LBUs = 2 or 3) forming no true glasses

Amorphous perovskites typically consist of 2–3 different types of LBUs, which can be either network formers or network modifiers (Figure 1B). Some of the best-studied examples (LBU = 2) include amorphous $BaTiO_3$, $SrTiO_3$, and $BaZrO_3$ perovskites.[29–32,52] In these structures, Ti or Zr octahedra have been identified as network formers connecting via shared corners, edges, and faces. In contrast, alkaline-earth-metal Ba or Sr cations have been observed to retard the transition from random bonding to corner-sharing polyhedral arrangements by stabilizing non-bridging oxygen for amorphous perovskites, serving as network modifiers. It is in fact the radii sizes within the amorphous network of the octahedral LBUs that determine whether they serve as a network modifier or network former. We wish to also highlight that these examples are by definition not Zachariasen glasses, as they have significantly higher-coordination (>4) octahedral LBUs. An intriguing aspect in these amorphous perovskite examples is that the LBUs (i.e., octahedra) arrange into a high variety of amorphous phases and condensation states through LBU connections, disruption, and reorganization, which affect macroscopic properties such as ionic transport and mechanics.[31] Consequently, the latter characteristics of the amorphous perovskite structures differ completely from those of Zachariasen glasses such as silica or non-Zachariasen invert glass such as LiPON in terms of their ability for LBU rearrangement into quasi-stable face- and edge-sharing CRNs.

We consider the amorphous $Li_{3x}La_{2/3-x}TiO_{3-\delta}$ (LLTO) battery electrolyte to be classified as similar based on LBUs > 2 (Figure 1B). Based on the structure information of previously studied amorphous $BaTiO_3$, $SrTiO_3$, and $BaZrO_3$ perovskites,[29–32] we classify the LBUs of LLTO as $[TiO_6]$ being the network former and $[LiO_{12}]$ and $[LaO_{12}]$ being most likely the network modifiers. Despite successful application in film synthesis,[36–38] its local structure and LBU connectivity have not yet been resolved, nor has the material been optimized toward Li-ion transport. This outcome is surprising, given its successful operations in battery with 4.8V $LiNi_{0.5}Mn_{1.5}O_4$ cathode[36] and technical success in excluding the highly resistive grain boundaries in the amorphous form, which greatly improved the power density and the CCD of LLTO-based batteries (Figure 1C).[53,54]

"Medium entropy" and high number of LBUs for solid-state conductors (LBUs $\geq$ 4) forming no true glasses

The local structure of amorphous Li-garnet phases remains unexplored and represents a case with the highest number of LBU arrangements known for an amorphous Li-ion conductor (Figure 1B). Applying the outlined nomenclature, we turn first to the crystalline LLZO polyhedra, which were identified earlier as containing four LBUs of $[LaO_8]$ dodecahedra, $[ZrO_6]$ and $[LiO_6]$ octahedra, and $[LiO_4]$ tetrahedra.[15,40] The amorphous garnet structures are believed to have a higher degree of complexity than the earlier outlined 2-LBU invert glasses (e.g., LiPON) or the 2- to 3-LBU examples of amorphous perovskites (e.g., LLTO) because the structural entropy is increased owing to the higher polyhedra variety. Only recently, in 2018, various amorphous Li-garnet phases were successfully synthesized[40]; however, their local ordering as well as the structural roles and connectivity of the four LBUs in determining the Li-ion conductivity remain unexplored. Specifically, it is unclear which LBUs act as network formers vs. network modifiers for amorphous Li-garnet phases.

Furthermore, unlike in the crystalline garnet phase, where Li mobility is driven by structural defects and vacancies, the Li-transport mechanism in this amorphous CRN remains unknown. Even though the structure is unresolved, it holds technological relevance for the battery field. Recently, a 10-nm-thick coating layer of amorphous Li garnet on a Li-garnet pellet electrolyte was demonstrated, successfully preventing Li-dendrite formation at remarkable current densities of up to 3.2 mA cm^{-2} (Figure 1C).[27] As a comparison point, the CCD reached for polycrystalline cubic Li garnet is usually approximately 0.6–1 mA cm^{-2}.[55–57] These findings suggest, even though the exact structure of the amorphous LLZO remains unresolved, that a grain-boundary-free protective layer could help to significantly enhance the CCD of batteries.

In essence, we collect evidence and descriptive factors for the structural nature of the medium-entropy amorphous Li-ion conductors, i.e., amorphous Li garnets, with an unusually high number of LBUs to alter Li motion. We define synthesis for various amorphous Li-garnet phases as a model material class, representing the highest number of known LBUs, namely four LBUs, in an amorphous Li-ion conductor. Unlike "low-entropy" amorphous Li-ion conductors, such as LiPON, amorphous Li garnets have a much wider temperature range to stabilize and tailor LBU arrangements and therefore control the Li motion. In addition, by gaining knowledge in this work through a wide combination of techniques, such as Raman spectroscopy, high-resolution transmission electron microscopy (HR-TEM), X-ray absorption spectroscopy (XAS), and nuclear magnetic resonance (NMR) spectroscopy, we deconvolute for the first time the types of LBU bonding and the definition of network formers and modifiers for these medium-entropy amorphous Li-ion conductors. Eventually, this work guides efforts toward more efficient and better-performing grain-boundary-free electrolytes or protective coatings for oxide- and sulfide-based full or hybrid solid-state batteries.

Structure and stability of the "medium-entropy" amorphous Li-garnet phases

Figures 2A and 2B present top-view and cross-sectional scanning electron microscopy (SEM) images of $Li_{6.25}Al_{0.25}La_3Zr_2O_{12}$ (LLZO, or Li-garnet) films processed using the new method of sequential decomposition synthesis (SDS)[58] at a deposition temperature of 300°C and are exemplified after post-annealing at 750°C for 15 min. The film presents an even coverage of the substrate with a relatively dense microstructure. The film thickness was measured to be 2.0 $\pm$ 0.3 μm. Raman spectroscopy was used to track the phase and lattice-vibrational evolution of the structure (Figure 2C). Specifically, *in situ* heating Raman measurement was selected to attain a better understanding of the phase and local structural transition at different temperatures. The broad Raman signal for the as-deposited film indicates the amorphous nature of the film, with the minor peak at 91 cm^{-1} (T_{2g} mode) attributable to O–La–O vibration. Upon heating to 750°C, more distinct peaks appeared, indicating phase transformation toward cubic-phase Li garnet. The peak centered at 240 cm^{-1} was assigned to the oxygen-bending band of T_{2g}/A_{1g},[59] and the uprising peaks centered at 368 and 468 cm^{-1} were assigned to the O–Li–O vibration bands (T_{2g} and E_g/T_{2g}) in LiO_6 octahedra.[60] In addition, the two intense peaks at 94 and 113 cm^{-1} are identified as T_{2g} and E_g mode of O–La–O vibration, and we also observe the O–Zr–O stretching band (A_{1g} mode) centered at 651 cm^{-1}.[59,60] To avoid thermal-induced noise and confirm the crystallization of Li garnet with better spectral resolution, we also recorded *ex situ* Raman spectra for the as-deposited film and the film after 750°C annealing (see detailed data and analysis in Figure S1). We confirm through the appearance of the Raman vibrational bands in both the *in situ*

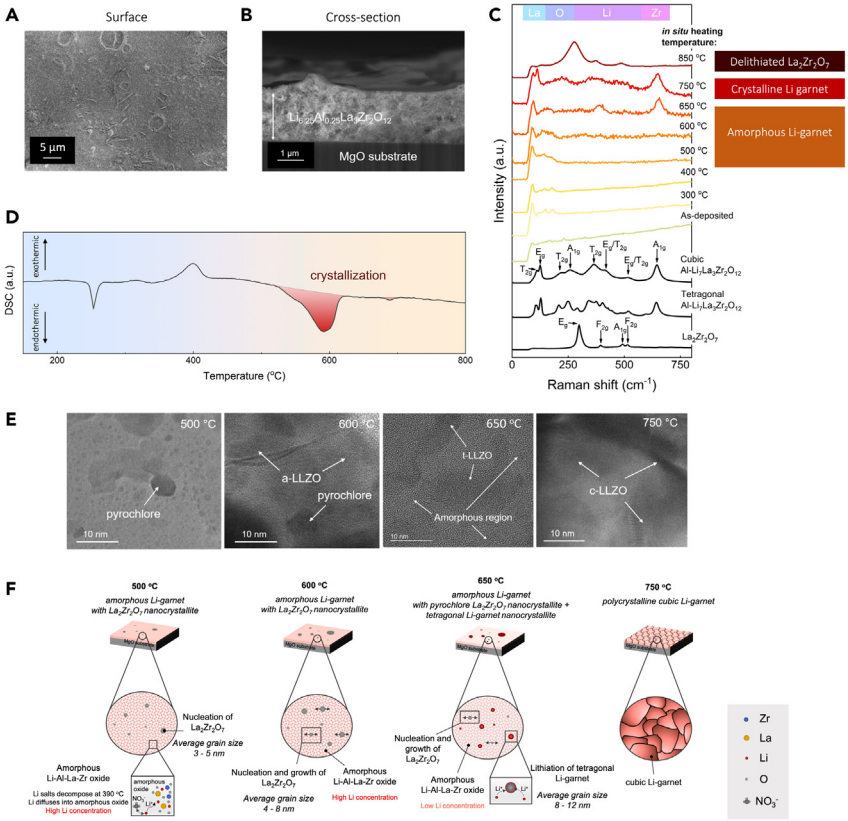


Figure 2. Structure and stability of amorphous Li-garnet films

(A) SEM surface image of SDS Li-garnet film annealed at 750°C.

(B) SEM cross-sectional image of SDS Li-garnet film annealed at 750°C.

(C) *In situ* heating Raman spectra for an SDS Li-garnet film measured from room temperature to 850°C at a heating rate of 5°C/min controlled by a Linkam stage under a constant flow of O_2. Reference spectra of cubic and tetragonal-phase LLZO and delithiated $La_2Zr_2O_7$ are also presented. The spectra indicate that the local structure of the film evolves with increasing temperature and that a fully crystalline film can be obtained at 750°C annealing. Further increasing the annealing temperature to 850°C will lead to significant delithiation with the formation of $La_2Zr_2O_7$. The film was prepared with 75% over-lithiation.

(D) Non-isothermal DSC of Li-garnet films prepared by SDS from 150°C to 800°C. The two peaks shaded in red correspond to amorphous local structure rearrangement and Li-garnet crystallization.

(E) *In situ* heating HR-TEM images of a Li-garnet film at 500°C, 600°C, 650°C, and 750°C.

(F) Schematics of phase evolution at 500°C, 600°C, 650°C, and 750°C. At 500°C, the film is composed of a lithiated amorphous Li-garnet phase with the nucleation of $La_2Zr_2O_7$ (grain size of 3–5 nm). At 600°C, nucleation and growth of $La_2Zr_2O_7$ continues with an average grain size of 4–8 nm. The majority of the film still remains amorphous Li garnet. At 650°C, while the nucleation and growth of $La_2Zr_2O_7$ continues, tetragonal Li-garnet nanocrystals are formed with lithiation of $La_2Zr_2O_7$. The migration of Li from the amorphous Li-garnet phase to tetragonal Li-garnet nanocrystals results in a low Li concentration in the remaining amorphous phase. At 750°C, the film is fully crystallized into cubic-phase Li garnet.

and *ex situ* spectra the formation of cubic-phase Li garnet at 750°C, and the amorphous nature of the as-deposited film.

Between the deposition temperature of 300°C and the crystallization temperature of 750°C, we observed ongoing phase evolution involving several amorphous states (i.e., polyamorphism). Upon heating from 300°C to 400°C, a more significant peak appears at 91 cm^{-1} for O–La–O T_{2g} vibration, and a few minor peaks are observed

between 100 and 250 cm^{-1}, which may be attributed to the T_{2g}/A_{1g} band characteristics for the oxygen bending (210 cm^{-1}).[59] Between 500°C and 600°C, an additional broad peak centered at 143 cm^{-1} is observed with a higher spectra noise level, which we identified as the merged peak of the emerging T_{2g}/A_{1g} band characteristic for the oxygen bending; the noise in the spectra may indicate an ongoing local structure evolution (i.e., rearrangement of LBUs). At 650°C, two new peaks at 389 and 656 cm^{-1} emerge, which can be correlated to the T_{2g} mode of O–Li–O vibration in LiO_6 octahedra[60] and the A_{1g} mode of O–Zr–O stretching,[59,60] respectively. We also observed that the spectral noise level is higher for peaks between 150 and 550 cm^{-1} (oxygen bending and O–Li–O vibration) and comparatively lower for peaks below 150 cm^{-1} (O–La–O vibration) and above 550 cm^{-1} (O–Zr–O stretching). This difference in spectra noise suggests that Li polyhedra and the corresponding Li–O bonds are more actively rearranging in the local structure at elevated temperature. At 850°C, however, a completely different spectrum with low noise level emerged. Three major peaks at 275, 374, and 491 cm^{-1} are observed, which can be correlated to the E_g mode, F_{2g} mode, and A_{1g}/F_{2g} modes of the (Li-loss) $La_2Zr_2O_7$ phase, respectively. The low spectral noise level observed in the spectrum also explains the complete loss of highly active Li (and the corresponding Li–O bonds).

Differential scanning calorimetry (DSC) is a well-established method used to study crystallization in glass ceramics, and we apply it here to further probe the occurrence of the amorphous-to-crystalline transformation of Li garnet observed in the *in situ* Raman spectra. The phase evolution was confirmed by DSC, with two endothermic peaks observed between 500°C and 720°C (Figure 2D), corresponding to the local structure rearrangement and the phase transition from amorphous to crystalline Li garnet. Detailed analysis of the reactions stemming from the initial SDS synthesis route can be found in Figure S2 and Hood et al.[58]

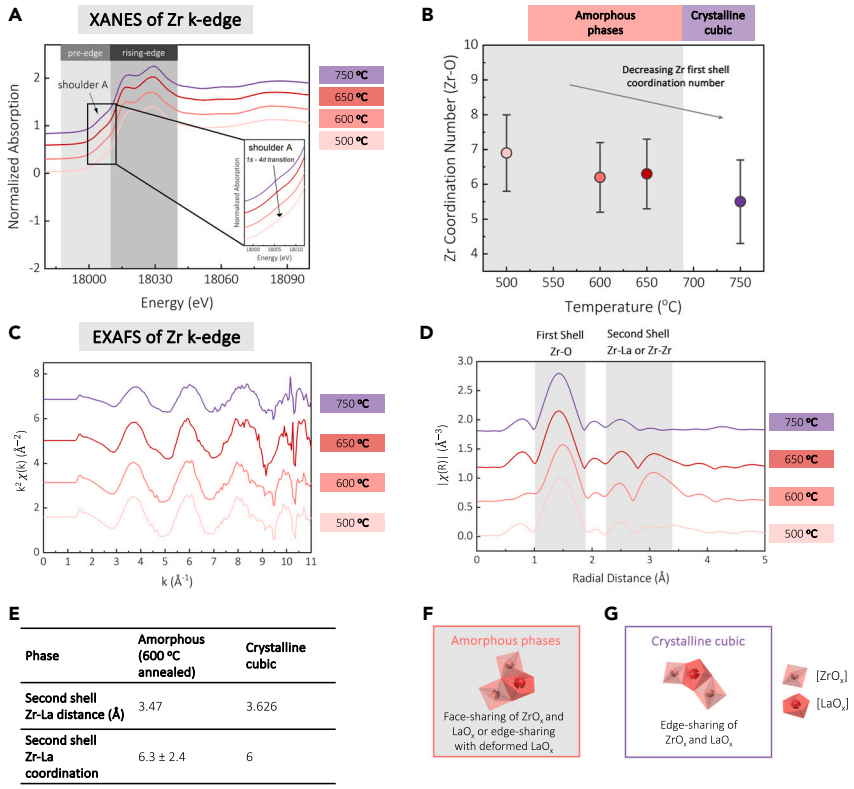
We used *in situ* HR-TEM to further explore the phase composition and nanostructure of the film during the amorphous-to-crystalline phase-transition process between 500°C and 750°C (Figure 2E), which is the phase-transition temperature range suggested by the *in situ* Raman spectroscopy and DSC analyses. The three representative microstructure images collected at 500°C, 600°C, and 650°C correspond to the different amorphous phases, and the one at 750°C corresponds to the cubic phase. At 500°C, an atomic-scale disordered structure with a few darker spots was observed in the HR-TEM image. A Fourier transform of the disordered region suggests a homogeneous amorphous film with no separate regions of a Li-rich phase (Figure S3A), indicating the successful lithiation of the amorphous film after the decomposition of Li-nitrate salt during the post-annealing process between 400°C and 500°C (Figure 2D), which is also supported by the DSC (see Figure S2 for details). A Fourier transform of the darker spots in the amorphous film indicates the presence of non-lithiated $La_2Zr_2O_7$ pyrochlore oxide nanocrystals with an average nuclei/grain size of 3–5 nm in (400) and $(1\bar{1}1)$ planes (Figure S3B). Increasing the post-annealing temperature to 600°C induces only a very minimal growth of the $La_2Zr_2O_7$ pyrochlore nanocrystals to an average grain size of 4–8 nm sitting in the predominantly amorphous and highly lithiated film (Figure S3B). The presence of $La_2Zr_2O_7$ pyrochlore nanocrystals agrees well with the minor $La_2Zr_2O_7$ pyrochlore peaks observed from *in situ* X-ray diffraction (XRD) between 500°C and 600°C in our earlier work.[58] It is only at a higher temperature of 650°C that changes in the phase nature and chemistry are observed in both the predominantly atomic-disordered amorphous structure and the isolated nanocrystalline grains. The crystalline grains grow to an average of 8–12 nm, but the Fourier transform indicates the presence of tetragonal-phase Li garnet in (101) and $(10\bar{1})$ planes (Figure S3C), indicating an ongoing

phase transformation and lithiation of the originally isolated pyrochlore to tetragonal Li-garnet nanocrystals in the still predominantly amorphous film. This observation also corroborates with the *in situ* XRD results reported in our earlier work, where minor XRD peaks corresponding to tetragonal Li garnet first appear at a temperature of 650°C.[58] Consequently, the amorphous phase must become Li-depleted as Li diffuses to the isolated pyrochlore grains in its matrix and thereby sets off the transformation to tetragonal Li-garnet phase in the nanocrystals. This is per se an interesting finding, as it suggests that the various amorphous phase states represent changes in their Li concentration, which can be tailored by the synthesis/post-annealing temperature and the isolated nuclei and nanocrystals. The differences in Li concentration and isolated nuclei types also affect Li-ion transport, which will be discussed in a later section. Finally, at 750°C, the film surpasses the amorphous states as it exhibits a high level of crystallinity with regions of uniform lattice fringes, as confirmed by the Fourier transform as cubic-phase Li garnet in $(11\bar{2})$, $(1\bar{1}2)$, and $(2\bar{2}0)$ planes (Figure S3D). The appearance of different plane orientations of the lattice fringes suggests the polycrystalline nature of the film with high crystallinity, which agrees well with the cubic phase observed at 750°C by *in situ* and *ex situ* Raman spectroscopy (Figures 2C andS1).

In conclusion, we confirmed with several independent spectroscopy, calorimetry, and microscopy methods that various and predominantly amorphous Li-garnet phases can be successfully synthesized and stabilized through the SDS method within a wide temperature window below 680°C. This result is technologically relevant, as the wide stability temperature window provides a vast amount of opportunities to alter the local structure and LBU arrangement for this medium-entropy amorphous material with four different LBUs. Comparatively, amorphous LiPON films can only be stabilized from room temperature to 280°C[3] and consist of only two LBUs. We found that the amorphous phases post-annealed between 500°C and 650°C must differ in their LBU arrangement and Li concentration according to the variation in Raman vibrational mode and intensity and the HR-TEM observation of different types and sizes of nanocrystals in the amorphous matrix. We also gained the first insight into the nucleation and growth steps in this medium-entropy amorphous material, whereby a temperature of 650°C is required to induce Li depletion in the amorphous phase and trigger Li diffusion to the pyrochlore nanocrystals, which then leads to the phase formation of tetragonal Li garnet and finally the crystallization of the whole film from tetragonal to cubic Li garnet. It is also important to mention that this knowledge about local phase evolution stems from a "liquid-to-solid" processing method that starts from a liquid precursor solution to a solid oxide film, which differs in nature from the classic solid-state synthesis route that begins with calcination of solid powders and requires a rather high temperature for sintering. To better understand the local structure of each LBU type and their arrangements, we next applied XAS and NMR spectroscopy to study the variation in Zr, La, and Li local environments among a wide range of non-Zachariasen amorphous Li-garnet phases.

Identifying the "network former and modifier" for a 4-LBU Li-ion conductor: The role of Zr and La

XAS is capable of detecting the local structure changes with high sensitivity and was selected to probe the local structure of the Zr LBU for the various amorphous vs. cubic crystalline Li-garnet films. Generally speaking, the X-ray absorption near-edge structure (XANES) region is sensitive to a wealth of electronic structure information, which can be used to determine the oxidation state and coordination number/geometry of the absorption atom. In addition to measuring the coordination numbers,



Phase	Amorphous (600 °C annealed)	Crystalline cubic
Second shell Zr-La distance (Å)	3.47	3.626
Second shell Zr-La coordination	6.3 ± 2.4	6

Figure 3. The role of Zr and La in local structure of amorphous Li garnets

(A) Zr K-edge XANES spectra of Li-garnet film processed at 500°C, 600°C, 650°C, and 750°C (shifted vertically for clarity). The spectra contain a pre-edge region for energy <18,010 eV and a rising-edge region for energy >18,010 eV. Inset: enlarged pre-edge region with increasing absorption in shoulder A, originating from 1*s*-to-4*d* transition.

(B) Best-fitted Zr coordination number of Li-garnet films in different amorphous and crystalline phases from EXAFS spectra. A gradually decreasing Zr coordination is fitted with increasing post-annealing temperature. The large fitting errors suggest a considerable variation in Zr local structure for all the phases.

(C) Zr K-edge EXAFS oscillation for the Li-garnet film processed at 500°C, 600°C, 650°C, and 750°C (shifted vertically for clarity).

(D) Fourier transform magnitudes of the k^2-weighted Zr K-edge EXAFS for the Li-garnet film processed at 500°C, 600°C, 650°C, and 750°C (shifted vertically for clarity). The peak regions corresponding to the Zr first-shell (Zr–O) and second-shell (Zr–La or Zr–Zr) bonding are highlighted. Error bars represent measurement uncertainites.

(E) Comparison of second-shell Zr–La distance and coordination number between amorphous (600°C annealed) and crystalline cubic phases.

(F and G) Schematic representation and corresponding LBU legends of the suggested ZrO_x and LaO_x connection in (F) amorphous (600°C annealed) and (G) crystalline cubic Li garnets.

the extended X-ray absorption fine structure (EXAFS) region of the spectrum can also provide information about bond distances between the absorption atoms and their nearest neighbors.

First, we evaluated the Zr K-edge XANES spectra in Figure 3A in two regions, namely, the pre-edge region (18,000–18,010 eV) and the rising-edge region (18,010–18,040 eV). The pre-edge region can be used to estimate the spin state and local symmetry, and the rising-edge region contains information about the charge state and coordination environment of the absorption atom. We observed a hump in the pre-edge region at ~18,007 eV and two major peaks in the rising-edge region centered at ~18,018 and

~18,031 eV in all the amorphous phases and the cubic one (Figure 3A). In the pre-edge region, the hump at ~18,007 eV, corresponding to the 1*s*-4*d* transition energy range, is usually denoted as shoulder *A* in Zr-containing glasses.[61] This transition is dipole forbidden in the atom by the ΔL = 1 selection rule.[62] Typically, the enhanced intensity in shoulder *A* indicates distortion of the Zr site by comparison with Zr-containing alkali silicate glasses, where Zr sits in symmetric octahedral sites.[63–65] Such an intensity increase is evidence of the *p*-*d* mixing via hybridization between O 2*p* and Zr 4*d* orbitals, a tell-tale sign of the deviation from the centrosymmetry.[66] In the 750°C annealed crystalline film (inset of Figure 3A), we see an increased intensity of shoulder *A* as compared with the lower-temperature amorphous films, which indicates an increasing Zr site distortion from the centrosymmetric octahedral sites (Figure 3A). In the rising-edge region, the two peaks centered at ~18,018 and ~18,031 eV are typically observed in Zr K-edge XANES spectra of Zr(IV)-containing glass-ceramic oxides, e.g., ZrO_2-SiO_2 glasses[63] and nanocrystalline ZrO_2,[67] indicating that Zr in all the samples is close to being octahedrally coordinated. Typically, higher coordination numbers cause absorption-edge maxima to be shifted to a lower energy and suggest a Zr coordination number larger than 6.[63,68] We fit the Zr K-edge EXAFS spectra and obtained a Zr coordination number of 6.9 ± 1.1, 6.2 ± 1.0, and 6.3 ± 1.0 for the amorphous Li-garnet films post-annealed at 500°C, 600°C, and 650°C, respectively, and 5.5 ± 1.2 for the 750°C annealed cubic one. We conclude that the Zr LBU exhibits a general decreasing trend on its coordination number with increasing post-annealing temperature (Figure 3B and Table S1). Compared to the coordination numbers for the three lower-temperature amorphous films, the aforementioned cubic phase has a smaller coordination number of <6. Both the distortion from centrosymmetric octahedral sites observed from the pre-edge XANES region and the under-coordination varied from the ideal octahedral LBU fitted from the EXAFS region suggest that the films possess a high local structure disorder with non-centrosymmetry, as opposed to the classic solid-state-processed ceramic pellets or tapes after sintering (see Chen et al.[69] for comparison).

Next, we turned to the EXAFS analysis of the next nearest neighbors to Zr. The EXAFS spectrum is shown as a function of the photoelectron wave number, *k* (Figure 3C). Fourier transform was performed for each k^2-weighted Zr K-edge EXAFS spectrum, and the magnitude of the Fourier transform was plotted as a function of the radial distance, *R* (Figure 3D). In a Fourier-transformed spectrum, the radial distances of the prominent peaks generally correspond to the bond distances between the near neighbors and the absorbing atoms, albeit the peak positions are shifted to the lower distances compared to the real space distances due to the photoelectron phase shift in EXAFS equation. Specifically, we observed two major peak regions in Figure 3D, with the first one sitting between 1.0 and 1.8 Å and the second one sitting between 2.2 and 3.4 Å, corresponding to the first- and second-shell neighbors to Zr, respectively. Next, to best determine the first-shell Zr–O distance in the complex amorphous system with five different elements, we performed fitting of the first-shell region of each Fourier-transformed spectrum in Figures S6–S9. The fittings indicated a decreasing trend of Zr–O radial distances of 2.12 ± 0.01 Å, 2.11 ± 0.01 Å, 2.10 ± 0.01 Å, and 2.10 ± 0.01 Å for amorphous films post-annealed at 500°C, 600°C, and 650°C, and the cubic one post-annealed at 750°C, respectively (Table S1).

The fitting analysis of the second shell of the Zr spectrum suggested that Zr–La contribution is sufficient for fitting the second shell, and the best-fit results are summarized in Figure 3E. Notably, the Zr–La distance in the exemplified 600°C amorphous film (3.47 Å) is significantly shorter than that corresponding to the edge-sharing units in the previously reported cubic-phase LLZO (3.626 Å).[70] We conclude from the fitting data of the second-shell Zr–La interaction that in

amorphous LLZO, LaO_x and ZrO_x are not edge sharing but possibly face shared (or that the LaO_x units are under-coordinated and deformed) (Figures 3F and 3G). This differs clearly from the edge-sharing ZrO_x and LaO_x in cubic Li garnet.

Collectively, we obtained several pieces of information about the Zr and La local structure from the XAS measurements. For the first-shell neighbor of Zr, we observed a decreasing trend for both the Zr–O distance and Zr–O coordination as crystallization progressed from 500°C to 750°C. For the second shell, we identified a higher second-shell Zr–La coordination and shorter second-neighbor La–Zr distances than that of the crystalline cubic Li garnet, indicating a possibly face-shared (or under-coordinated and deformed) LBU connection among LaO_x and ZrO_x (Figures 3F and 3G). Here, we identify Zr as a network former, as the Zr LBU shares edges and faces with neighboring LBUs in different amorphous and crystalline phases, promoting the formation of a CRN. On the contrary, we identify La as a network modifier that alters the CRN and retards the crystallization, as La has a large atomic radius and is 8-fold coordinated, which prevents thermodynamically stable connection with 6- or 4-fold coordinated LBUs. Doping at the La site with low-coordination dopants can be a potential strategy to alter and stabilize the CRN in amorphous Li garnets. To better understand the role of Li in local structure evolution, we next applied ^{7}Li NMR to probe the Li coordination and short-range ordering in amorphous and crystalline Li garnets.

Understanding local Li disorder and Li dynamics

^{7}Li NMR measurements are highly sensitive to the Li coordination and short-range ordering. Here, ^{7}Li NMR was used to characterize both the various amorphous states (i.e., post-annealing at 500°C, 600°C, and 650°C) and cubic one (post-annealed at 750°C) of Li garnets. Magic-angle spinning (MAS) ^{7}Li NMR spectra were collected to study the chemical shift (δ) behavior in terms of the mean value and distribution width, the latter being a possible indicator of the degree of local structure disorder (Figure 4A). Narrower peaks in MAS spectra suggest a higher degree of local structural ordering; in contrast, a broader peak could be the result of slight differences in local Li environments leading to a wider distribution of chemical shifts and thus indicating higher disorder around Li. The position of ^{7}Li resonances is indicative of the Li coordination number and previous studies on, e.g., Li-containing phosphate glasses also indicate a possible correlation between lower chemical shift and higher Li–O coordination numbers.[71]

From ^{7}Li MAS NMR measurement, we observed a significantly narrower peak for the cubic Li garnet than for the various amorphous Li-garnet phases (Figure 4A). Specifically, a full width at half maximum (FWHM) of 1.012 $\pm$ 0.009 kHz was obtained from the cubic film, compared to FWHM of 1.168 $\pm$ 0.014 kHz, 1.207 $\pm$ 0.009 kHz, and 1.187 $\pm$ 0.011 kHz obtained from the amorphous Li-garnet phases annealed at 500°C, 600°C, and 650°C, respectively (Figures 4A and 4B; Table S2). Within the amorphous phases, the FWHM showed an initial increase and peaked for the 600°C post-annealed Li garnet, followed by a sharp decrease for the cubic sample (750°C post-annealed), exhibiting a narrower peak with a more Lorentzian than Gaussian line shape (Figure 4B). Because contributions from dipolar coupling are averaged out under MAS, and a significant contribution from broadening due to second-order quadrupolar coupling can be dismissed, we attribute the linewidth in these ^{7}Li MAS spectra to a distribution of chemical-shift values. This interpretation is corroborated by the Gaussian contribution to line shape of ^{7}Li lines for samples annealed below 650°C. The width of this distribution, and hence the FWHM of the ^{7}Li MAS NMR signal, should reflect the disorder in Li local environments. We

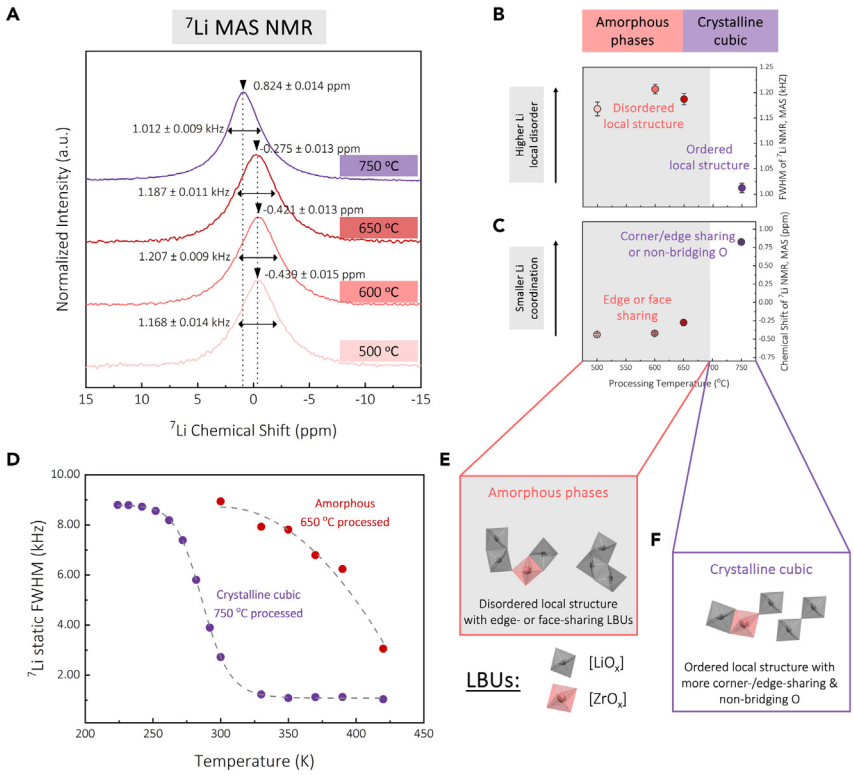


Figure 4. Li coordination and short-range ordering

(A) ^{7}Li MAS NMR spectra for Li-garnet film annealed at 500°C, 600°C, 650°C, and 750°C.

(B) FWHM of ^{7}Li chemical shifts from MAS NMR spectra. With increasing annealing temperature, a Lorentzian line shape is observed with the largest FWHM for the 600°C annealed film and smallest FWHM for the 750°C annealed film (crystalline cubic). The small fitting errors indicate that the changes are significant. Error bars represent the uncertainities of FWHM based on noise contribution and were estimated by determining their variation across 100 samples of random points from the spectra.

(C) Changes of ^{7}Li chemical shift of MAS NMR spectra. With increasing annealing temperature, a monotonic increase in chemical shift is observed. The small fitting errors indicate that the changes in the chemical shifts are significant. Error bars represent the uncertainties of chemical shift based on noise contribution and were estimated by determining their variation across 100 samples of random points from the spectra.

(D) FWHM of ^{7}Li VT NMR for 650°C annealed amorphous Li garnet and 750°C annealed crystalline cubic Li garnet.

(E and F) Schematic representation and corresponding LBU legends of the suggested Li local structure in (E) amorphous and (F) crystalline cubic Li garnets.

conclude that all amorphous Li-garnet phases exhibit larger disorder than the crystalline cubic Li garnet, with the maximum degree of structural disorder observed for the 600°C annealed film.

In addition, we noted an increase of the chemical shift (δ) from the 500°C post-annealed amorphous Li-garnet sample to the cubic Li-garnet sample (Figure 4A). Specifically, δ of -0.439 ± 0.015 ppm, -0.421 ± 0.013 ppm, -0.275 ± 0.013 ppm, and 0.824 ± 0.014 ppm were measured for the amorphous Li garnet annealed at 500°C, 600°C, and 650°C and the cubic one annealed at 750°C, respectively (Figures 4A and 4C; Table S3). Previous studies of Li-containing phosphate and silicate glasses[71,72] have indicated that lower δ generally suggests a larger Li coordination. For Li garnets, the increase in δ could indicate a decreasing Li coordination from amorphous to crystalline phases. In this study, Li coordination can be regarded as

Li–O bonding coordination because of the oxide nature of the material, which precludes direct cation interactions. Among the amorphous samples, negative δ ranged from −0.44 ppm (for 500°C Li garnet) to −0.27 ppm (for 650°C Li garnet), suggesting larger Li–O coordination. Conversely, the cubic sample exhibited a positive δ of 0.82 ppm, which implies a significantly different and overall smaller Li–O coordination environment than the amorphous ones. This suggests that possibly more Li LBUs in amorphous phases are 6-fold coordinated (exist as LiO_6) as compared to the 1:2 ratio of the 4- and 6-fold coordinated Li LBUs (existing as LiO_4 and LiO_6, respectively) in cubic Li garnet. Similar to the Zr coordination and LBU connection changes suggested by the XAS analysis, we rationalize that the comparatively larger Li–O coordination in amorphous phases based on the interpretation of the NMR spectra may suggest either deformed LiO_x polyhedra or edge- and face-oxygen sharing of LiO_x polyhedra with other LBUs (Figures 4E and 4F).

To further explore the Li-transport dynamics and deconvolute peak-narrowing causes (chemical-shift distributions and motional narrowing), we also performed ^{7}Li variable temperature (VT) NMR for the cubic and 650°C annealed amorphous Li-garnet phases (Figure 4D) without MAS. For the cubic Li-garnet example, a typical motional line narrowing is observed from 224 K to 420 K (Figures 4D andS10), similar to the dynamics observed in the previously reported cubic Al-doped Li garnet.[73] Also, this coincides with a steep decrease in linewidth between 250 K and 300 K (Figure S10). In contrast, the exemplary amorphous Li-garnet presents a less steep transition from the rigid to mobile lattice regime, which starts at 300 K and is not yet fully narrowed at 420 K (Figures 4D and S11). The different line-narrowing behavior observed in static VT NMR can be interpreted as a broader distribution of local Li environments with varying Li mobilities for the amorphous sample and corroborates the observation of linewidth from MAS spectra. Although VT NMR spectra were not recorded for all amorphous samples, it is likely that they are also within the rigid lattice regime at room temperature. Similar peak widths were observed in the ^{7}Li static NMR spectra for the amorphous films (Figure S12), with the FWHM varying in the range of approximately 7.3–7.5 kHz (Table S4 and Figure S13). This contrasts sharply with the linewidth of 3.074 kHz for the 750°C annealed cubic Li garnet recorded under the same conditions, for which the onset of motional narrowing lies below room temperature (Figure 4D).

In essence, we conclude that amorphous Li garnets possess the following characteristics from the ^{7}Li NMR analysis. First, all the studied amorphous Li-garnet phases present greater structure disorder than the cubic phase, based on the FWHM of ^{7}Li MAS NMR spectra. Second, among the various amorphous phases studied here, we observe variation in Li local structure disorder with the highest degree of Li local disorder for the 600°C post-annealed film, suggesting a generally looser LBU arrangement with higher structural entropy. Third, various amorphous Li-garnet phases potentially possess increased Li–O coordination, as inferred from the ^{7}Li chemical-shift values, suggesting either deformed LiO_x polyhedra or edge- and face-sharing LiO_x polyhedra with other LBUs as a part of the CRN. Importantly, this finding differs substantially from the classic Zachariasen glass formation rules where Li, with small atom radius, are generally considered as a network modifier or an interstitial ion in the CRN but not as a network former. Nevertheless, this result aligns with the LBU connections as suggested by the independent EXAFS analysis, where ZrO_x and LaO_x are either face shared or under-coordinated and deformed. Fourth, amorphous and crystalline Li garnets exhibit clearly different Li-transport dynamics. The earlier motional narrowing onset temperature for the cubic sample in VT NMR suggests a generally faster local Li-ion motion. This trend is in line with the later and less steep onset for motional narrowing of ^{7}Li NMR lines upon heating for the

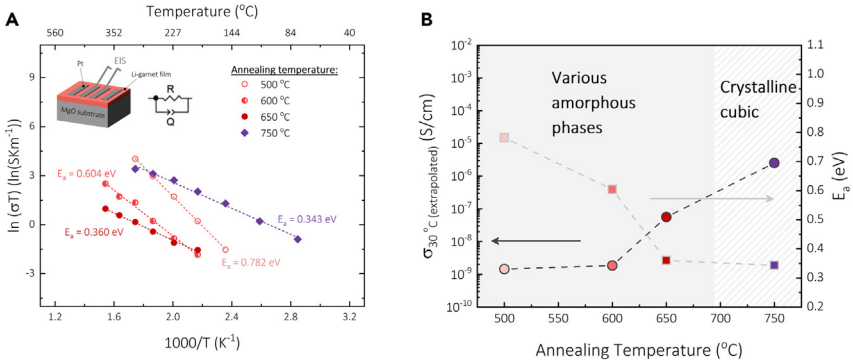


Figure 5. Li-transport behavior in amorphous vs. crystalline Li-garnet films

(A) Arrhenius representation of Li-ion conductivity measured for Li-garnet films annealed at 500°C, 600°C, 650°C, and 750°C. Inset left: schematic representation of in-plane EIS measurement on a Li-garnet film. Inset right: resistor-constant phase element equivalent circuit model used for fitting. (B) Calculated activation energy and extrapolated room-temperature conductivity (30°C) as a function of the annealing temperature for the Li-garnet films.

amorphous sample, which implies a broader distribution of Li-ion dynamics as a consequence of the higher structural disorder of Li, Zr, and La LBUs.

Li-ion transport in "medium-entropy" Li garnets and battery integration perspectives

Electrochemical impedance spectroscopy (EIS) was selected to study Li-transport behavior in the amorphous and crystalline Li-garnet films. All the EIS spectra were collected with an in-plane geometry (inset of Figure 5A), and a resistor-constant phase element equivalent circuit model (inset of Figure 5A) was used for fitting (see Figures S14 and S15 for more details). We display in Figure 5A an Arrhenius representation for the Li-ion conductivities measured among the various amorphous and cubic Li-garnet films. The films exhibited room-temperature Li-ion conductivities of 1.44×10^{-9}, 1.85×10^{-9}, and 5.59×10^{-8} S cm^{-1} for the various amorphous phases post-annealed at 500°C, 600°C, and 650°C, respectively, and 2.51×10^{-6} S cm^{-1} for the cubic one. The minimum of activation energy is found from the amorphous phase post-annealed at 650°C and the cubic phase at 0.360 and 0.343 eV, respectively (Figures 5A and 5B; Table S5). The other lower-temperature annealed amorphous phases reveal rather high activation energies up to 0.78 eV. The variation in activation energy agrees with the line-narrowing behavior observed in VT NMR, where we observed a broader distribution of local Li environments with varying Li mobilities in amorphous films. For the cubic Li-garnet film, the improved ion transport corresponds to the formation of a long-range-order structure, which lowers the activation-energy barrier for Li-ion hopping (see Figure S16 for more detailed analysis). It is also worth noting that the ionic conductivity of the cubic Li-garnet film obtained in this study agrees well with the previously reported conductivity values from the SDS-processed Li-garnet films[58] and films deposited using other wet-chemical methods,[74–76] which are generally lower in Li-ion conductivity compared with bulk Li-garnet pellets or tapes.[3,77] The reduced conductivity can be related to the Li loss at elevated temperature during the deposition or the post-processing steps or the high grain-boundary-to-grain-bulk volume ratio (generally, grain boundaries have lower Li-ion conductivities), which is commonly observed for almost all solid-state Li-oxide conductors.[3,77] Importantly, we believe this structure-property understanding of the 4-LBU amorphous Li garnets can not only benefit the fundamental materials science for medium-entropy amorphous oxides but also brings new opportunities for next-generation battery electrolyte

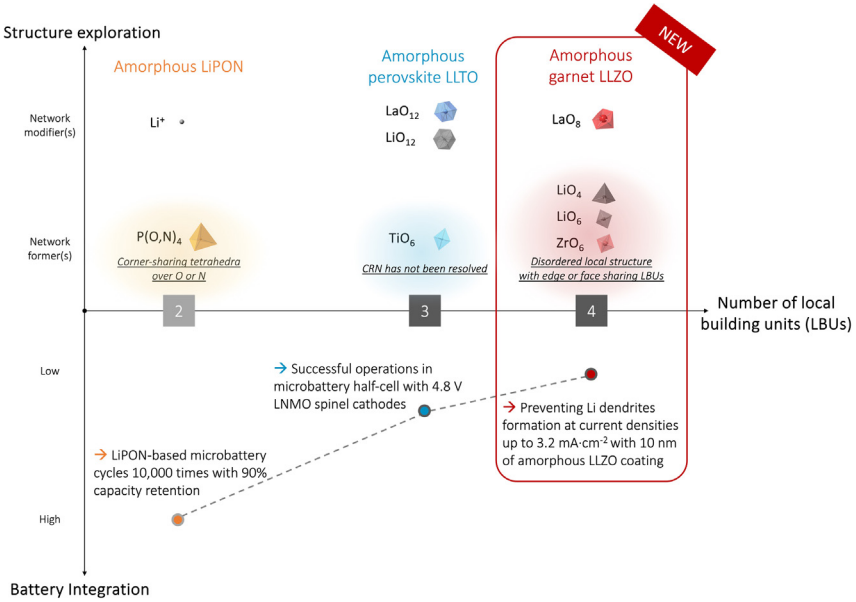


Figure 6. Roadmap for the recent advancement of amorphous Li solid-battery electrolytes
The summary includes progress of the local structure exploration and battery integration for amorphous LiPON, amorphous perovskite LLTO, and amorphous garnet LLZO.

advancement (Figure 6). Compared with LiPON, which has only two LBUs of $P(O,N)_4$ and Li^+, and the amorphous perovskite LLTO, which has three LBUs of TiO_6, LaO_{12}, and LiO_{12}, amorphous Li garnet sits in a unique position with medium structural entropy of four different LBUs. This structure offers vast opportunities to tune the chemistry and CRN of the material, e.g., by doping on the network modifier site, to further improve the transport properties. In terms of battery applications of amorphous oxide-based electrolytes, LiPON thus far represents the highest level of battery performance with the best-performing microbattery cycled over 10,000 times with less than 10% capacity loss.[23] Comparatively, amorphous LLTO shows less progress in terms of battery integration. It was only in 2016 that a microbattery half-cell with an amorphous LLTO solid-state electrolyte and a high-voltage (4.8 V) LNMO spinel cathode was demonstrated.[36] Even later, in 2021, the first amorphous Li-garnet-based microbattery was demonstrated with amorphous Li garnet acting as a solid-electrolyte separator layer, successfully cycled at 10 C for over 500 cycles; the same study also reported the use of a 10-nm amorphous Li garnet as a coating layer on cubic Li-garnet pellet, preventing Li-dendrite formation up to 3.2 mA cm^{-2}.[27] This outstanding battery performance already achieved in this early stage of the field justifies the potential of such medium-entropy amorphous Li-garnet conductors with new opportunities waiting to be discovered. With both experimental and simulation efforts, we see a vast space ahead for further optimizing the structure, conduction, and battery integration of medium-entropy amorphous Li garnets.

Conclusions

Next-generation hybrid and solid-state batteries rely on electrolyte materials to guarantee good chemical and electrochemical stability at interfaces to avoid the formation of high-resistance interfacial layers and the growth of Li dendrites. This article illustrates a class of medium-entropy amorphous Li-ion conductors, namely amorphous Li garnets with the highest number of LBUs (≥ 4) identified so far, that can be stabilized over a wide thermal processing window at low temperatures. We propose a sorting metric to the battery field by contextualizing this material class

toward other "low-entropy" amorphous Li electrolytes based on the numbers and types of network formers and network modifiers and their LBU hierarchy. A multi-faceted investigation has been carried out to resolve the structure of these medium-entropy amorphous Li-garnet phases, to identify major roles of the LBUs, and to understand their implications for Li dynamics. Specifically, we observed edge- and face-shared LiO_x, LaO_x, and ZrO_x LBUs in amorphous Li-garnet phases presenting much higher structural entropy than the solely corner-shared LiPON conductor with only two types of LBU. In addition, the higher-entropy edge- and face-sharing CRNs in amorphous Li garnets offer wider opportunities to tune the ion transport as compared to the quasi-stable amorphous perovskites with three LBUs. Within these amorphous Li-garnet phases, Li and Zr have been identified as network formers and La as network modifier, with the highest Li-ion conductivity observed for films with smaller Li–O and Zr–O coordination. These findings set the cornerstone for developing novel structure modulation strategies, e.g., doping the network modifier La site or tuning Li concentration, to further influence the Li-ion dynamics.

With a low but wide temperature window to stabilize the various amorphous states and the ability to access multiple CRNs via structure modulation, we see opportunities for medium-entropy Li-ion conductors to play different roles in both hybrid (i.e., liquid-electrolyte) and solid-state (i.e., oxide- or sulfide-based electrolyte) batteries. In hybrid and sulfide-based solid-state batteries, the amorphous Li garnets can be applied as a thin protective layer on a Li-metal anode to bridge the stability voltage gap and reduce the risk of uneven Li deposition and local strain formation in polycrystalline cubic Li garnets while minimizing the subsequent growth of Li dendrites. In addition, in oxide-based solid-state batteries the amorphous Li garnets can be used as the active electrolyte layer with the advantage of reduced thermal processing budget (<680°C), therefore eliminating the need for a high-temperature co-sintering step with cathodes. This is significant, as it improves the accessibility to a wider selection of Co-reduced or even Co-free cathodes (e.g., $LiNiMnCoO_2$, $LiNiCoAlO_2$, and $LiFePO_4$), which often show limited chemical compatibility with oxide-based electrolytes at a temperature above 700°C.

Finally, this work demonstrates a successful protocol for describing the CRN of these medium-entropy amorphous Li-ion conductors with four unique LBUs, investigating some of the many phases present and describing the local bond, coordination, Li environments, and LBU connections. While this work is primarily focusing on the role of major LBUs in amorphous Li garnets, we anticipate further attention on the role of various network modifiers (i.e., new dopant series) and Li concentration and their implications on transport properties. Considering the two decades it has taken LiPON to successfully resolve the CRN and tune the Li dynamics to the optimum, research on medium-entropy amorphous Li garnets is still at an early stage. We anticipate additional experimental and computational efforts on amorphous Li garnets in the next 5–10 years to achieve their best performance. In particular, the high number of LBUs ($\geq$4) within amorphous Li garnets offers a much wider opportunity to tune the structure and transport properties than the 2-LBU amorphous LiPON. Given the good cell performance recently reported with amorphous Li garnets employed both as electrolyte separators and protective layers without much structure optimization, we see promise and significance of our contribution here serving as a blueprint for structure and phase modulation to enable hybrid or solid-state battery designs with further enhanced safety, energy density, and lifetime.

EXPERIMENTAL PROCEDURES

Resource availability

Lead contact

Further information and requests for resources should be directed to and will be fulfilled by the lead contact, Jennifer L.M. Rupp (jrupp@mit.edu or jrupp@tum.de).

Materials availability

The new phases of amorphous Li garnets generated in this study are available from the lead contact.

Data and code availability

The data that support the findings of this study are available from the corresponding author upon reasonable request. Full details of experimental procedures can be found in supplemental information.

Preparation of amorphous-to-crystalline solid-state Li-garnet films by SDS

The SDS precursor solution was prepared in the $Li_{6.25}Al_{0.25}La_3Zr_2O_{12}$ stoichiometric ratio with 75 mol % extra Li by dissolving $LiNO_3$, $Al(NO_3)_3 \cdot 9H_2O$, $La(NO_3)_3 \cdot 6H_2O$, and zirconium(IV) acetylacetonate into methanol:1-methoxy-2-propanol:bis(2-ethylhexyl) phthalate (1:1:1 vol. %) solvent. Our previous study[1] suggested that including a 75 mol % excess of Li in the SDS precursor solution can lead to the successful synthesis of cubic Li-garnet phase with the highest Li-ion conductivity and relatively high film density. Thus, 75 mol % of excess Li was used for the SDS solution preparation in this work as a model case. There is room to further optimize the Li concentration to achieve improved transport properties for amorphous Li garnets. The concentration of the solution was 0.015 M. All the SDS solutions were stirred overnight for at least 12 h before use for SDS. $LiNO_3$ (≥99%), zirconium(IV) acetylacetonate (97%), and 1-methoxy-2-propanol (≥99.5%) were purchased from Sigma-Aldrich; $Al(NO_3)_3 \cdot 9H_2O$, $La(NO_3)_3 \cdot 6H_2O$ (99.99%), and bis(2-ethylhexyl) phthalate were purchased from Alfa Aesar; and methanol was purchased from VWR. Because Li garnet does not react with MgO, single-side-polished MgO (001) substrates (10 × 10 × 0.5 mm) were purchased from MTI and used as the substrate for the SDS process.

To deposit the Li-garnet electrolyte film, the MgO substrates were placed on a heated stainless-steel hot plate at 300°C with the polished side facing up. A K-type thermocouple was placed on the side of the MgO substrate to monitor the temperature of the substrate surface. During deposition, the SDS solution was transferred from a polypropylene syringe and pumped at a rate of 10 mL h^{-1} into a spray atomizer (DeVILBLISS, AG361). Compressed gas with a pressure of 0.3 bar at the atomizer was used as the carrier gas for the deposition. The distance between the spray atomizer and MgO substrate was maintained at 25 cm throughout the deposition. For all the films studied in this work, a thickness of 2 μm was achieved with 1-h deposition. After deposition, the films were post-annealed in an alumina crucible in a temperature-calibrated tube furnace between 500°C and 750°C under a flow of pure O_2 (Airgas) with a ramp rate of 5°C min^{-1}. The post-annealed films were stored inside an Ar-filled glovebox before measurements to prevent potential exposure to ambient air and moisture and to minimize chemical degradation.

Phase, thin-film chemistry, and microstructure characterization

The local phase structure of the Li-garnet films was characterized using Raman spectroscopy (WITec alpha 300 M+). A laser wavelength of 532 nm was applied with a power of 10 mW, a grating of 300 g mm^{-1}, and a spectral resolution of 0.1 cm^{-1}

to obtain all the Raman data presented in the paper. A 50× long-distance objective (Zeiss, Germany) with a numerical aperture of 0.7 was used for the laser focusing, giving an approximate laser spot size of 1 μm. A Linkam TS1500 stage was used as the temperature- and atmosphere (synthetic air)-controlled stage for *in situ* heating measurements from room temperature to 850°C (calibrated actual temperature) with a heating rate of 5°C min^{-1}.

Surface and cross-sectional SEM images of the deposited Li-garnet films were collected with a Zeiss Supra55VP field-emission scanning electron microscope using an accelerating voltage of 3.0–10.0 kV. An in-lens SE detector and Everhart-Thornley SE detector were used for SEM image collection for all the samples in this study. For the cross-sectional samples, a diamond blade was used to cut the sample before imaging. Conductive carbon tape was used to tape the sides of the samples to ensure sufficient electronic conductivity during imaging.

Thermal properties characterization and crystallization kinetics analysis

The sample for the DSC experiments was collected in powder form by scratching off the as-deposited films from MgO substrates. MgO crucibles (Ozark Technical Ceramics) were selected for the DSC experiments to avoid high-temperature reaction and diffusion between the Li garnet and crucibles. Since the as-deposited amorphous Li garnets were processed via a wet-chemical SDS method without the presence of Mg precursors during deposition, the tendency of Mg diffusion from MgO crucibles/substrates to Li-garnet films is low. Furthermore, we have confirmed in our previous work[1] through the X-ray photoelectron spectroscopy depth profile of an SDS-processed Li-garnet film that there was no measurable Mg in the post-annealed film. The experiments were performed using a Mettler Toledo Thermal Analysis System TGA/DSC 3+ under a constant flow of synthetic air from room temperature to 1,000°C with a ramp rate of 10°C min^{-1}. A constant flow of Ar (Airgas) was used as protective gas during the experiments.

In situ transmission electron microscopy

HR-TEM was performed on an aberration-corrected FEI Titan S 8-300 transmission/scanning transmission electron microscope equipped with a Gatan Image Filter Quantum-865 operated at 300 kV. The specimens were prepared by depositing films via SDS (thicknesses of 50–80 nm) onto an MEMS-based heating chip (Protochips). A Protochips Aduro heating holder was used for all the *in situ* heating experiments. The specimens were heated at a rate of 20°C/min with isothermal dwells of 0.5–60 min to evaluate the atomistic evolutions during the post-processing of the films. The electron beam was carefully tuned to minimize any electron-beam-induced damage to the films. All TEM images and data were post-processed using DigitalMicrograph (Gatan Microscopy Suite) software.

Local ordering structure characterization

EXAFS/XANES fluorescence Zr K-edge XAS was performed for the post-annealed Li-garnet films at beamline 20-BM of the Advanced Photon Sources. The samples were deposited on MgO substrates and sealed in a vacuum bag before conducting the experiments to minimize surface contamination due to air exposure. The fluorescence mode was selected as it can penetrate through the entire layer of the Li-garnet film, which minimizes the effect of possible surface contamination caused by air exposure (i.e., Li_2CO_3 formation). The measurement on each sample was repeated five times, and the averaged spectrum was used for data analysis.

Athena software, a part of the Demeter software suite,[2] was used for data analysis and linear combination fitting. The collected XAS spectra were normalized in

intensity for better comparison. The model for data analysis had the amplitude factor fixed to 0.79, obtained from the Zr foil analysis. The Zr-O coordination number and the distance and disorder parameters were varied in the fit, along with the energy origin correction. In the first-shell region, the data were analyzed concurrently with the same energy correction.

Room-temperature ^{7}Li MAS NMR spectra were obtained on a Bruker 700-MHz (16.4-T) magnet with an Avance III console using a Bruker 1.3-mm HXY MAS probe. An MAS rate of 10 kHz was applied to avoid sample heating due to friction. A single-pulse sequence with a total of four scans was used, with a recycle delay of 100 s, using the appropriate Ernst angle as a compromise for long spin-lattice relaxation times (on the order of 100 s). The spectra were externally referenced against Li_2CO_3 powder (0 ppm).[3]

Static VT ^{7}Li NMR spectra were acquired on a Bruker 500-MHz (11.8-T) magnet with an Avance III console using a Bruker 4-mm HFXY MAS probe in static mode. The spectra were externally referenced against LiCl saturated aqueous solution (0 ppm).[3] High-temperature NMR spectra were measured between 300 K and 420 K after an equilibration time of at least 20 min after each temperature was reached where heated nitrogen gas was used as heating source. Low-temperature NMR spectra were measured between 224 K and 292 K using nitrogen gas and a Bruker cooling unit (BCU-II). Powdered $Pb(NO_3)_2$ was used for temperature calibration.[4]

A regular zg/one-pulse pulse program was used to obtain the spectra using flip angles of $\leq \pi/2$ (2 μs). All the samples were packed in 1.3-mm (MAS NMR) or 4-mm (static VT NMR) ZrO_2 rotors under an Ar atmosphere inside a glovebox (M. Braun; $p(O_2)/p0 < 1$ ppm, $p(H_2O)/p^0 < 1$ ppm). Bruker Topspin 3.5 pL7,[5] Mestrenova 11.0.0, and Origin 2019 were used for raw data handling and processing. The uncertainties for the FWHM and chemical shift were based on noise contribution and were estimated by determining their variation across 100 samples of random points from the spectra.

Electrochemical characterization

The Li-ion conductivity of the SDS Li-garnet thin films was measured with in-plane geometry by EIS (Zahner IM6). Platinum-blocking electrodes (3 mm in length with a separation distance of 0.25 mm) were deposited on the Li-garnet films using a Cressington 108 Auto sputter coater with a stainless-steel shadow mask. The measurement was conducted with gold-coated tungsten tips. A temperature- and atmosphere-controlled Linkam HFS-600E stage was used for the measurements, with a thermocouple placed directly on the membrane surface to rectify the temperature profile. An AC amplitude of 50 mV was applied with frequencies between 1 MHz and 0.1 Hz. For each film, an impedance spectrum was obtained every 50°C from 100°C to 500°C (set temperature) with 2-min stabilization time for two consecutive heating and cooling cycles to ensure measurement accuracy. All the impedance measurements were performed under a constant flow of dry synthetic air. The collected data were analyzed using ZView 3.4F.

SUPPLEMENTAL INFORMATION

Supplemental information can be found online at https://doi.org/10.1016/j.matt.2023.12.004.

ACKNOWLEDGMENTS

Y.Z. acknowledges financial support provided by the MIT Energy Initiative fellowship offered by ExxonMobil. Y.Z. and Z.D.H. acknowledge financial support provided by Samsung Electronics. M.B. acknowledges financial support provided by the US-Israel

Fulbright Program, the Zuckerman Israeli Postdoctoral Scholar Program, and the MIT-Technion Postdoctoral Fellowship. P.B.G. acknowledges financial support provided by the German Academic Exchange Service (DAAD) for the PRIME fellowship and the Dutch Research Council (NWO) for the ECCM Tenure Track funding under project number ECCM.006. F.N.S. would like to acknowledge the Faraday Institution CATMAT project (grant number FIRG016) for the funding. S.P.E. acknowledges funding provided by ERC project no. 835073 (BATNMR). Data analysis of X-ray absorption spectroscopy by A.I.F. was supported by NSF grant number DMR-1911592. I.L. acknowledges the BSF program grant 2018717 for his contribution to the these studies. These grants are the two parts of the NSF-BSF grant awarded to A.I.F. and I.L., respectively. J.L.M.R. thanks the Thomas Lord Foundation for financial support. M.B. and J.L.M.R. wish to thank the Bavarian Ministry of Economic Affairs, Regional Development and Energy for funding the research project "Industrialisierbarkeit von Festkörperelektrolytzellen." This research was performed in part at the Center for Nanoscale Systems (CNS), a member of the National Nanotechnology Coordinated Infrastructure Network, which was supported by the National Science Foundation under NSF award no. 1541959. CNS is a part of Harvard University. This research used resources of the Advanced Photon Source, an Office of Science User Facility operated for the US Department of Energy (DOE) Office of Science by Argonne National Laboratory, and was supported by the US DOE under contract no. DE-AC02-06CH11357, and the Canadian Light Source and its funding partners. The TEM characterization was performed at the Center for Nanophase Materials Sciences, which is a DOE Office of Science User Facility. The authors would also like to thank Prof. Christopher A. Schuh's lab at MIT for offering access and providing support for the DSC experiments.

AUTHOR CONTRIBUTIONS

Y.Z. and J.L.M.R. proposed the concept of "medium-entropy" amorphous Li-ion conductors and the classification of existing and newly identified amorphous Li-ion conductors. Y.Z. and J.L.M.R. designed the experiments. Y.Z., Z.D.H., L.J.M., and J.L.M.R. discussed the ceramic processing and phase evolution data. Y.Z. and H.P. performed the EIS measurements. Z.D.H. collected the HR-TEM images. Y.Z. and C.S. performed the XAS experiments. Y.Z., I.L., J.L.M.R., and A.I.F. discussed and performed the data analysis for the XAS experiments. S.P.E., P.B.G., F.N.S., and C.P.G. designed and performed the NMR experiments and analysis. Y.Z. and J.L.M.R. wrote the manuscript with the help of all co-authors.

DECLARATION OF INTERESTS

J.L.M.R. is on the advisory board of *Matter*.

Received: August 14, 2023
Revised: November 8, 2023
Accepted: December 7, 2023
Published: January 9, 2024

REFERENCES

1. Kim, K.J., Hinricher, J.J., and Rupp, J.L.M. (2020). High energy and long cycles. Nat. Energy *5*, 278–279.

2. Janek, J., and Zeier, W.G. (2016). A solid future for battery development. Nat. Energy *1*, 16141.

3. Balaish, M., Gonzalez-Rosillo, J.C., Kim, K.J., Zhu, Y., Hood, Z.D., and Rupp, J.L.M. (2021). Processing thin but robust electrolytes for solid-state batteries. Nat. Energy *6*, 227–239.

4. Bauer, C., Burkhardt, S., Dasgupta, N.P., Ellingsen, L.A.W., Gaines, L.L., Hao, H., Hischier, R., Hu, L., Huang, Y., Janek, J., et al. (2022). Charging sustainable batteries. Nat. Sustain. *5*, 176–178.

5. Xu, W., Wang, J., Ding, F., Chen, X., Nasybulin, E., Zhang, Y., and Zhang, J.G. (2014). Lithium metal anodes for rechargeable batteries. Energy Environ. Sci. *7*, 513–537.

6. Albertus, P. (2016). Integration and Optimization of Novel Ion-Conducting Solids (IONICS) Funding Opportunity Announcement. https://arpa-e-foa.energy.gov/FileContent.aspx?FileID=cfac9ce8-5a19-4623-b942-c3e65f3ccf77.

7. Swamy, T., Park, R., Sheldon, B.W., Rettenwander, D., Porz, L., Berendts, S., Uecker, R., Carter, W.C., and Chiang, Y.M. (2018). Lithium Metal Penetration Induced by Electrodeposition through Solid Electrolytes: Example in Single-Crystal $Li_6La_3ZrTaO_{12}$ Garnet. J. Electrochem. Soc. *165*, A3648–A3655.

8. Buschmann, H., Dölle, J., Berendts, S., Kuhn, A., Bottke, P., Wilkening, M., Heitjans, P., Senyshyn, A., Ehrenberg, H., Lotnyk, A., et al. (2011). Structure and dynamics of the fast lithium ion conductor "$Li_7La_3Zr_2O_{12}$.". Phys. Chem. Chem. Phys. *13*, 19378–19392.

9. Afyon, S., Krumeich, F., and Rupp, J.L.M. (2015). A shortcut to garnet-type fast Li-ion conductors for all-solid state batteries. J. Mater. Chem. A. Mater. *3*, 18636–18648.

10. Allen, J.L., Wolfenstine, J., Rangasamy, E., and Sakamoto, J. (2012). Effect of substitution (Ta, Al, Ga) on the conductivity of $Li_7La_3Zr_2O_{12}$. J. Power Sources *206*, 315–319.

11. Wolfenstine, J., Ratchford, J., Rangasamy, E., Sakamoto, J., and Allen, J.L. (2012). Synthesis and high Li-ion conductivity of Ga-stabilized cubic $Li_7La_3Zr_2O_{12}$. Mater. Chem. Phys. *134*, 571–575.

12. Liu, Q., Geng, Z., Han, C., Fu, Y., Li, S., He, Y. bing, Kang, F., and Li, B. (2018). Challenges and perspectives of garnet solid electrolytes for all solid-state lithium batteries. J. Power Sources *389*, 120–134.

13. Murugan, R., Thangadurai, V., and Weppner, W. (2007). Fast lithium ion conduction in garnet-type $Li_7La_3Zr_2O_{12}$. Angewandte Chemie - International Edition *46*, 7778–7781.

14. Zhu, Y., Chon, M., Thompson, C.V., and Rupp, J.L.M. (2023). Time–Temperature–Transformation (TTT) Diagram of Battery-Grade Li-Garnet Electrolytes for Low-Temperature Sustainable Synthesis. Angew. Chem. Int. Ed. *62*, e202304581.

15. Johnson, R.T., Biefeld, R.M., Knotek, M.L., Morosin, B., Kennedy, J.H., Yang, Y., Mercier, R., Malugani, J.P., Fahys, B., Robert, G., et al. (2018). A Stable Thin-Film Lithium Electrolyte: Lithium Phosphorus Oxynitride. Solid State Ion *1*, 173–178.

16. Bates, J.B., Dudney, N.J., Gruzalski, G.R., Zuhr, R.A., Choudhury, A., Luck, C.F., and Robertson, J.D. (1993). Fabrication and characterization of amorphous lithium electrolyte thin films and rechargeable thin-film batteries. J. Power Sources *43*, 103–110.

17. Cheng, E.J., Sharafi, A., and Sakamoto, J. (2017). Intergranular Li metal propagation through polycrystalline $Li_{6.25}Al_{0.25}La_3Zr_2O_{12}$ ceramic electrolyte. Electrochim. Acta *223*, 85–91.

18. Han, F., Westover, A.S., Yue, J., Fan, X., Wang, F., Chi, M., Leonard, D.N., Dudney, N.J., Wang, H., and Wang, C. (2019). High electronic conductivity as the origin of lithium dendrite formation within solid electrolytes. Nat. Energy *4*, 187–196.

19. Liu, X., Garcia-Mendez, R., Lupini, A.R., Cheng, Y., Hood, Z.D., Han, F., Sharafi, A., Idrobo, J.C., Dudney, N.J., Wang, C., et al. (2021). Local electronic structure variation resulting in Li 'filament' formation within solid electrolytes. Nat. Mater. *20*, 1485–1490.

20. Cho, J.H., Kim, K., Chakravarthy, S., Xiao, X., Rupp, J.L.M., and Sheldon, B.W. (2022). An Investigation of Chemo-Mechanical Phenomena and Li Metal Penetration in All-Solid-State Lithium Metal Batteries Using In Situ Optical Curvature Measurements. Adv. Energy Mater. *12*, 2200369.

21. Dixit, M.B., Vishugopi, B.S., Zaman, W., Kenesei, P., Park, J.S., Almer, J., Mukherjee, P.P., and Hatzell, K.B. (2022). Polymorphism of garnet solid electrolytes and its implications for grain-level chemo-mechanics. Nat. Mater. *21*, 1298–1305.

22. Zhu, Y., Balaish, M., and Rupp, J.L.M. (2022). Uncovered Phase Polymorphism Steers Chemo-Mechanics of Garnet Electrolytes. Joule *6*, 2680–2682.

23. Li, J., Ma, C., Chi, M., Liang, C., and Dudney, N.J. (2015). Solid electrolyte: The key for high-voltage lithium batteries. Adv. Energy Mater. *5*, 1401408.

24. Schwobel, A., Hausbrand, R., and Jaegermann, W. (2015). Interface reactions between LiPON and lithium studied by in-situ X-ray photoemission. Solid State Ion *273*, 51–54.

25. Cheng, D., Wynn, T.A., Wang, X., Wang, S., Zhang, M., Shimizu, R., Bai, S., Nguyen, H., Fang, C., Kim, M. cheol, et al. (2020). Unveiling the Stable Nature of the Solid Electrolyte Interphase between Lithium Metal and LiPON via Cryogenic Electron Microscopy. Joule *4*, 2484–2500.

26. Hood, Z.D., Chen, X., Sacci, R.L., Liu, X., Veith, G.M., Mo, Y., Niu, J., Dudney, N.J., and Chi, M. (2021). Elucidating Interfacial Stability between Lithium Metal Anode and Li Phosphorus Oxynitride via in Situ Electron Microscopy. Nano Lett. *21*, 151–157.

27. Sastre, J., Futscher, M.H., Pompizi, L., Aribia, A., Priebe, A., Overbeck, J., Stiefel, M., Tiwari, A.N., and Romanyuk, Y.E. (2021). Blocking lithium dendrite growth in solid-state batteries with an ultrathin amorphous Li-La-Zr-O solid electrolyte. Commun Mater *2*, 1–10.

28. Zhu, Y., He, X., and Mo, Y. (2016). First principles study on electrochemical and chemical stability of solid electrolyte-electrode interfaces in all-solid-state Li-ion batteries. J Mater Chem A Mater *4*, 3253–3266.

29. Wachtel, E., and Lubomirsky, I. (2010). Quasi-amorphous inorganic thin films: Non-crystalline polar phases. Adv. Mater. *22*, 2485–2493.

30. Ehre, D., Cohen, H., Lyahovitskaya, V., and Lubomirsky, I. (2008). X-ray photoelectron spectroscopy of amorphous and quasiamorphous phases of $BaTiO_3$ and $SrTiO_3$. Phys. Rev B Condens Matter Mater Phys. *77*, 184106.

31. Ehre, D., Cohen, H., Lyahovitskaya, V., Tagantsev, A., and Lubomirsky, I. (2007). Structural transformations during formation of quasi-amorphous $BaTiO_3$. Adv. Funct. Mater. *17*, 1204–1208.

32. Lyahovitskaya, V., Feldman, Y., Zon, I., Wachtel, E., Gartsman, K., Tagantsev, A.K., and Lubomirsky, I. (2005). Formation and thermal stability of quasi-amorphous thin films. Phys Rev B Condens Matter Mater Phys *71*, 094205.

33. Lacivita, V., Westover, A.S., Kercher, A., Phillip, N.D., Yang, G., Veith, G., Ceder, G., and Dudney, N.J. (2018). Resolving the Amorphous Structure of Lithium Phosphorus Oxynitride (Lipon). J. Am. Chem. Soc. *140*, 11029–11038.

34. Lacivita, V., Artrith, N., and Ceder, G. (2018). Structural and Compositional Factors That Control the Li-Ion Conductivity in LiPON Electrolytes. Chem. Mater. *30*, 7077–7090.

35. Senevirathne, K., Day, C.S., Gross, M.D., Lachgar, A., and Holzwarth, N.A.W. (2013). A new crystalline LiPON electrolyte: Synthesis, properties, and electronic structure. Solid State Ion *233*, 95–101.

36. Lee, J.Z., Wang, Z., Xin, H.L., Wynn, T.A., and Meng, Y.S. (2016). Amorphous Lithium Lanthanum Titanate for Solid-State Microbatteries. J. Electrochem. Soc. *164*, A6268.

37. Furusawa, S.I., Tabuchi, H., Sugiyama, T., Tao, S., and Irvine, J.T.S. (2005). Ionic conductivity of amorphous lithium lanthanum titanate thin film. Solid State Ion *176*, 553–558.

38. Li, C.L., Zhang, B., and Fu, Z.W. (2006). Physical and electrochemical characterization of amorphous lithium lanthanum titanate solid electrolyte thin-film fabricated by e-beam evaporation. Thin Solid Films *515*, 1886–1892.

39. Belous, A.G., Novitskaya, G.N., Polyanetskaya, S. v, and Gornikov, Y.I. (1987). Study of complex oxides with the composition $La_{2/3-x}Li_{3x}TiO_3$. Inorg. Mater. *23*, 412.

40. Garbayo, I., Struzik, M., Bowman, W.J., Pfenninger, R., Stilp, E., and Rupp, J.L.M. (2018). Glass-Type Polyamorphism in Li-Garnet Thin Film Solid State Battery Conductors. Adv. Energy Mater. *8*, 1702265.

41. Kalita, D.J., Lee, S.H., Lee, K.S., Ko, D.H., and Yoon, Y.S. (2012). Ionic conductivity properties of amorphous Li-La-Zr-O solid electrolyte for thin film batteries. Solid State Ion *229*, 14–19.

42. Shelby, J.E. (2005). Introduction to Glass Science and Technology, 2nd ed (Royal Society of Chemistry).

43. Chen, S., Xie, D., Liu, G., Mwizerwa, J.P., Zhang, Q., Zhao, Y., Xu, X., and Yao, X. (2018). Sulfide solid electrolytes for all-solid-state lithium batteries: Structure, conductivity, stability and application. Energy Storage Mater. *14*, 58–74.

44. Saienga, J., and Martin, S.W. (2008). The comparative structure, properties, and ionic conductivity of LiI + Li_2S + GeS_2 glasses doped with Ga_2S_3 and La_2S_3. J. Non-Cryst. Solids *354*, 1475–1486.

45. Kumar, G., Desai, A., and Schroers, J. (2011). Bulk metallic glass: The smaller the better. Adv. Mater. *23*, 461–476.

46. Moskovskikh, D., Vorotilo, S., Buinevich, V., Sedegov, A., Kuskov, K., Khort, A., Shuck, C., Zhukovskyi, M., and Mukasyan, A. (2020). Extremely hard and tough high entropy nitride ceramics. Sci. Rep. *10*, 1–8.

47. Oses, C., Toher, C., and Curtarolo, S. (2020). High-entropy ceramics. Nat. Rev. Mater. *5*, 295–309.

48. Calahoo, C., and Wondraczek, L. (2020). Ionic glasses: Structure, properties and classification. J. Non-Cryst. Solids X *8*, 100054.

49. Mani, P.D., Saraf, S., Singh, V., Real-Robert, M., Vijayakumar, A., Duranceau, S.J., Seal, S., and Coffey, K.R. (2016). Ionic conductivity of bias sputtered lithium phosphorus oxy-nitride thin films. Solid State Ion *287*, 48–59.

50. Mascaraque, N., Fierro, J.L.G., Durán, A., and Muñoz, F. (2013). An interpretation for the increase of ionic conductivity by nitrogen incorporation in LiPON oxynitride glasses. Solid State Ion *233*, 73–79.

51. López-Grande, A., Dagupati, R., Galán del Sastre, P., and Muñoz, F. (2021). Ionic conductivity of Li_2O–P_2O_5 glasses from thermodynamic modeling of their chemical structure. J. Am. Ceram. Soc. *104*, 5625–5635.

52. Hashimoto, T., and Moriwake, H. (2020). Structure of amorphous $BaTiO_3$ by molecular dynamics simulations using a shell model. Physica B Condens Matter *579*, 411799.

53. Ma, C., Chen, K., Liang, C., Nan, C.W., Ishikawa, R., More, K., and Chi, M. (2014). Atomic-scale origin of the large grain-boundary resistance in perovskite Li-ion-conducting solid electrolytes. Energy Environ. Sci. *7*, 1638–1642.

54. Wu, J.F., and Guo, X. (2017). Origin of the low grain boundary conductivity in lithium ion conducting perovskites: $Li3_xLa0.6_{7-x}TiO_3$. Phys. Chem. Chem. Phys. *19*, 5880–5887.

55. Sharafi, A., Haslam, C.G., Kerns, R.D., Wolfenstine, J., and Sakamoto, J. (2017). Controlling and correlating the effect of grain size with the mechanical and electrochemical properties of $Li_7La_3Zr_2O_{12}$ solid-state electrolyte. J Mater Chem A Mater *5*, 21491–21504.

56. Kim, K.J., Balaish, M., Wadaguchi, M., Kong, L., and Rupp, J.L.M. (2021). Solid State Batteries: Solid-State Li–Metal Batteries: Challenges and Horizons of Oxide and Sulfide Solid Electrolytes and Their Interfaces. Adv. Energy Mater. *11*, 2002689.

57. Tsai, C.L., Roddatis, V., Chandran, C.V., Ma, Q., Uhlenbruck, S., Bram, M., Heitjans, P., and Guillon, O. (2016). $Li_7La_3Zr_2O_{12}$ Interface Modification for Li Dendrite Prevention. ACS Appl. Mater. Interfaces *8*, 10617–10626.

58. Hood, Z.D., Zhu, Y., Miara, L.J., Chang, W.S., Simons, P., and Rupp, J.L.M. (2022). A Sinter-Free Future for Solid-State Battery Designs. Energy Environ. Sci. *15*, 2927–2936.

59. Larraz, G., Orera, A., and Sanjuán, M.L. (2013). Cubic phases of garnet-type $Li_7La_3Zr_2O_{12}$: The role of hydration. J Mater Chem A Mater *1*. 11419–1142.

60. Tietz, F., Wegener, T., Gerhards, M.T., Giarola, M., and Mariotto, G. (2013). Synthesis and Raman micro-spectroscopy investigation of $Li_7La_3Zr_2O_{12}$. Solid State Ion *230*, 77–82.

61. Mastelaro, V.R., and Zanotto, E.D. (2018). X-ray Absorption Fine Structure (XAFS) studies of oxide glasses-A 45-year overview. Materials *11*, 204.

62. Stern, E.A., and Heald, S.M. (1983). In Handbook on Synchrotron Radiation, *Vol. 1* (E.E. Koch North-Holland).

63. Dargaud, O., Calas, G., Cormier, L., Galoisy, L., Jousseaume, C., Querel, G., and Newville, M. (2010). In situ study of nucleation of zirconia in an MgO-Al_2O_3-SiO_2 glass. J. Am. Ceram. Soc. *93*, 342–344.

64. Farges, F., Ponader, C.W., and Brown, G.E. (1991). Structural environments of incompatible elements in silicate glass/melt systems: I. Zirconium at trace levels. Geochim Cosmochim Acta *55*, 1563–1574.

65. Ferlat, G., Cormier, L., Thibault, M.H., Galoisy, L., Calas, G., Delaye, J.M., and Ghaleb, D. (2006). Evidence for symmetric cationic sites in zirconium-bearing oxide glasses. Phys Rev B Condens Matter Mater Phys *73*, 214207.

66. Grunes, L.A. (1983). Study of the K edges of the 3d transition metals in pure and oxide form by x-ray-absorption spectroscopy. Phys. Rev. B *27*, 2111.

67. Li, P., Chen, I.W., and Penner-Hahn, J.E. (1993). X-ray-absorption studies of zirconia polymorphs. I. Characteristic local structures. Phys. Rev. B *48*, 10063.

68. Brown, G.E., Calas, G., Waychunas, G.A., and Petiau, J. (2019). X-ray absorption spectroscopy and its applications in mineralogy and geochemistry. In Spectroscopic Methods in Mineralogy and Geology (De Gruyter).

69. Chen, Y.T., Jena, A., Pang, W.K., Peterson, V.K., Sheu, H.S., Chang, H., and Liu, R.S. (2017). Voltammetric Enhancement of Li-Ion Conduction in Al-Doped $Li_{7-x}La_3Zr_2O_{12}$ Solid Electrolyte. J. Phys. Chem. C *121*, 15565–15573.

70. Chen, Y., Rangasamy, E., Liang, C., and An, K. (2015). Origin of High Li^+ Conduction in Doped $Li_7La_3Zr_2O_{12}$ Garnets. Chem. Mater. *27*, 5491–5494.

71. Alam, T.M., Conzone, S., Brow, R.K., and Boyle, T.J. (1999). 6Li, 7Li nuclear magnetic resonance investigation of lithium coordination in binary phosphate glasses. J. Non-Cryst. Solids *258*, 140–154.

72. Xu, Z., and Stebbins, J.F. (1995). 6Li nuclear magnetic resonance chemical shifts, coordination number and relaxation in crystalline and glassy silicates. Solid State Nucl. Magn. Reson. *5*, 103–112.

73. Posch, P., Lunghammer, S., Berendts, S., Ganschow, S., Redhammer, G.J., Wilkening, A., Lerch, M., Gadermaier, B., Rettenwander, D., and Wilkening, H.M.R. (2020). Ion dynamics in Al-Stabilized $Li_7La_3Zr_2O_{12}$ single crystals – Macroscopic transport and the elementary steps of ion hopping. Energy Storage Mater. *24*, 220–228.

74. Tadanaga, K., Egawa, H., Hayashi, A., Tatsumisago, M., Mosa, J., Aparicio, M., and Duran, A. (2015). Preparation of lithium ion conductive Al-doped $Li_7La_3Zr_2O_{12}$ thin films by a sol-gel process. J. Power Sources *273*, 844–847.

75. Bitzer, M., van Gestel, T., Uhlenbruck, S., and Hans-Peter-Buchkremer. (2016). Sol-gel synthesis of thin solid $Li_7La_3Zr_2O_{12}$ electrolyte films for Li-ion batteries. Thin Solid Films *615*, 128–134.

76. Chen, R.J., Huang, M., Huang, W.Z., Shen, Y., Lin, Y.H., and Nan, C.W. (2014). Sol-gel derived Li-La-Zr-O thin films as solid electrolytes for lithium-ion batteries. J Mater Chem A Mater *2*, 13277–13282.

77. Zhu, Y., Gonzalez-Rosillo, J.C., Balaish, M., Hood, Z.D., Kim, K.J., and Rupp, J.L.M. (2021). Lithium-film ceramics for solid-state lithionic devices. Nat. Rev. Mater. *6*, 313–331.